In situ synchrotron X-ray diffraction characterization of corrosion products of a Ti-based metallic glass for implant applications

Gostin, Petre Flaviu; Addison, Owen; Morrell, Alexander P; Zhang, Yue; Cook, Angus J M C; Liens, Alethea; Stoica, Mihai; Ignatyev, Konstantin; Street, Steven R; Wu, Jing; Chiu, Yu-Lung; Davenport, Alison J

DOI:
10.1002/adhm.201800338

WILEY-VCH

DOI: 10.1002/ ((please add manuscript number))
Article type: Full Paper

In Situ Synchrotron X-Ray Diffraction Characterization of Corrosion Products of a Ti-Based Metallic Glass for Implant Applications

Petre Flaviu Gostin, Owen Addison, Alexander P. Morrell, Yue Zhang, Angus Cook, Alethea Liens, Mihai Stoica, Konstantin Ignatyev, Steven Richard Street, Jing Wu, Yu-Lung Chiu, and Alison J. Davenport**

Dr. P. F. Gostin, Prof. O. Addison, Y. Zhang, A. Cook, Dr. S. R. Street, J. Wu, Dr. Y. L. Chiu, Prof. A. J. Davenport
School of Metallurgy and Materials (O. Addison, School of Dentistry), University of Birmingham, Edgbaston, Birmingham B15 2TT, United Kingdom
E-mail: flaviu.g@outlook.com
E-mail: a.davenport@bham.ac.uk
Alexander Morrell
Aston Institute of Materials Research, Aston University, Birmingham, B4 7ET, United Kingdom
Alethea Liens
Université de Lyon, INSA-Lyon, Laboratoire MATEIS, UMR CNRS 5510, 20 Avenue Albert Einstein, 69621 Villeurbanne Cedex, France
Dr. Mihai Stoica
Laboratory of Metal Physics and Technology, Department of Materials, ETH Zürich, 8093 Zürich, Switzerland
Dr. Konstantin Ignatyev
Diamond Light Source, Harwell Science and Innovation Campus, Didcot, Oxfordshire OX11 0DE, United Kingdom

Keywords: metallic biomaterials, bulk metallic glasses, corrosion, in situ synchrotron X-ray diffraction, artificial pits

Ti-based bulk metallic glasses are under consideration for implants due to their high yield strength and biocompatibility. In this work, in situ synchrotron X-ray diffraction (XRD) has been used to investigate the corrosion products formed from corrosion of $Ti_{40}Zr_{10}Cu_{34}Pd_{14}Sn_2$ bulk metallic glass in artificial corrosion pits in physiological saline (NaCl). It was found that Pd nanoparticles form in the interior of the pits during electrochemical dissolution. At a low pit growth potential, the change in lattice parameter of the Pd nanoparticles is consistent with the formation of palladium hydride. In addition, a salt layer very close to the dissolving

interface was found to contain CuCl, $PdCl_2$, $ZrOCl_2 \cdot 8H_2O$, Cu, Cu_2O and several unidentified phases. The formation of Pd nanoparticles (16 ± 10 nm at 0.7 V vs Ag/AgCl) containing small amounts of the other alloying elements was confirmed by transmission electron microscopy. The addition of albumin and/or H_2O_2 does not significantly influence the nature of the corrosion products. When considering the biological compatibility of the alloy, the biological reactivity of the corrosion products identified should be explored.

1. Introduction

Metallic implants are commonly comprised of crystalline commercial pure Ti (cp-Ti) or Ti alloys, e.g. Ti6Al4V.[1] While these perform well in many implant applications, their mechanical strength can be insufficient for small implant components that are subjected to large functional forces, e.g. dental implants with diameters less than 3 mm. Owing to their high yield strength, bulk metallic glasses (BMG) that can be cast in shapes with diameters >1 mm are ideal candidates for these types of implants as well as larger load-bearing prosthetics.[2] Additionally, their high hardness may be a positive factor in reducing the rate of mechanically-assisted crevice corrosion (MACC), which can take place when there is microscopic vibration of a tight crevice between the metal and another surface such as metal, bone or cement.[3]

Some of the most promising Ti-based BMGs for small implant applications are in the Ti-Zr-Cu-Pd-(Sn) system. These BMGs have yield strengths exceeding 2 GPa (compared with 1 GPa for Ti6Al4V).[4] Recently, it was shown that small dental implants and their associated abutments can be manufactured from one alloy in this system, i.e. $Ti_{40}Zr_{10}Cu_{36}Pd_{14}$ (at. %), via a subtractive machining route, routinely used in the dental implant industry.[5] In vivo studies have demonstrated that a similar alloy, $Ti_{40}Zr_{10}Cu_{34}Pd_{14}Sn_2$, has equivalent bone integration and bonding ability to cp-Ti.[6] Conventional polarisation curves showed that

alloys in the Ti-Zr-Cu-Pd-(Sn) family have excellent passivity in simulated physiological solutions and relatively high pitting resistance. [2b, 7]

Analysis of tissues associated with failed implants have shown for many alloys and applications that corrosion has occurred which may not have been predicted by standard corrosion testing. For example, Addison et al.[8] found evidence of Ti debris in ex-vivo tissues surrounding a bone-anchored hearing aid (cp-Ti) which was attributed to corrosion. The corrosion resistance of Ti is due to the formation of a passive TiO_2 film on its surface. While current standard testing focuses on the stability of the passive surface against breakdown, e.g.[9], clinically many implant failures have been associated with 'mechanically-assisted crevice corrosion' (MACC).[3] MACC takes place when an implant component is in tight contact with another component, cement or bone. Small vibrations damage the protective oxide film, enabling metal dissolution and subsequent acidification, which in turn weakens the oxide film and accelerates corrosion in the gap. In this process solid corrosion products and metal fragments can also be produced and accumulate in the neighbouring tissue potentially influencing processes leading to implant failure. Therefore, it is necessary to understand the nature of all corrosion products and test their biocompatibility prior to implementation of any new Ti alloy.

It is essential to characterise corrosion products in situ as these are expected to change significantly if removed from the highly acidic crevice solution. However, such an experiment poses major technical challenges. Instead, in this work, corrosion products are generated in artificial pits. The artificial pit method is an established method for fundamental studies of pitting corrosion.[10] An artificial pit consists of a thin wire or foil embedded in an inert material which is electrochemically dissolved to a sufficient depth in a relevant chloride-containing solution. A sufficiently high potential is applied so that the dissolution rate of the metal is higher than the diffusion rate of its cations out of the pit cavity, leading to the formation of a metal chloride salt layer at the dissolving metal surface that simulates

conditions in real pits. Additionally, insoluble corrosion products may form and accumulate in the pit cavity. It can be seen that MACC and (artificial) pits both involve active dissolution in occluded geometries limiting outward diffusion. It could therefore be expected that similar corrosion products are generated, especially if dissolution takes place at similar potentials. Indeed, Monir found anatase-TiO_2, rutile-TiO_2 and Ti metallic fragments in artificial pits on Ti, which were also found in ex vivo tissues which once surrounded failed implants.[11] Recent investigations have revealed that albumin and H_2O_2 have a synergistic deleterious effect on the corrosion of Ti6Al4V in physiological saline.[12] This is associated with the formation of Ti-peroxy complexes and interaction of albumin with the corrosion products. Therefore, it is possible that albumin (the prevalent protein in extra-cellular tissue fluid) and H_2O_2 (which represents a reactive oxygen species formed in inflammatory processes) may also influence the formation of corrosion products on Ti alloys.

In this paper, in situ synchrotron X-ray diffraction (XRD) is used to identify and characterize corrosion products generated in artificial pits on the $Ti_{40}Zr_{10}Cu_{34}Pd_{14}Sn_2$ metallic glass in physiological saline (0.9% NaCl) with or without additions of 4% albumin and 0.1% H_2O_2. Ex situ transmission electron microscopy was also used to characterise the corrosion products formed. Special focus is placed on metallic corrosion products as these pose risk of accumulation in the peri-implant tissue. Conclusive evidence of the formation of metallic Pd nanoparticles was found. At lower potentials, relevant for service conditions, Pd nanoparticles might absorb hydrogen generated cathodically. Additionally, evidence for the formation of CuCl, $PdCl_2$, $ZrOCl_2{\cdot}8H_2O$, Cu and Cu_2O was found.

2. Results

2.1. In situ characterization of corrosion products with XRD

2.1.1. Corrosion products at 1.3 V

Figure 1a shows an optical microscope image of an artificial pit grown in 0.9% NaCl at 1.3 V after ~5 h growth and prior to X-ray measurements. The pit cavity is filled with black corrosion products. Figure 1b shows diffraction patterns taken at the points in line 'A' in Figure 1a. Points 1-4 show the background scattering from the solution path above the mouth of the pit above the black region. Points 5-15 show peaks that correspond to those of standard bulk metallic Pd shown at the top of the figure. They vary in intensity. The diffraction rings associated with Pd are continuous and uniform indicating they have a random crystallographic orientation (see Figure S1 in Supporting Information). Calculation with the Scherrer formula results in a crystallite size of 6.8 ± 0.9 nm.[13] Close to the interface (point 17), the most intense Pd peak (111) is not clearly distinguishable from the main scattering halo of the metallic glass (points 17-21). However, other Pd reflections, e.g. 022, are clearly visible showing that Pd is also present in that region. Close to the interface, additional diffraction peaks indicate the presence of other crystalline phases, $PdCl_2$ (points 15 and 16) and CuCl (point 18). Rings associated with CuCl have a narrow width and contain spots indicating that CuCl crystallites are much larger (see Figure S1 in Supporting Information). Points 18-21 show scattering from the metallic glass foil at 18, 30 and 36°.

Figure 1c shows a finer stack plot of X-ray diffraction patterns close to the interface corresponding to line 'B' in Figure 1a. Again, the outer region (points 1-15) is predominantly Pd. Closer to the interface, points 16-53 show a mixture of Pd and $PdCl_2$. Below this layer, there is a region (points 55-67) where the peaks attributed to $PdCl_2$ fade. Instead, Pd is present with two unknown phases 'X1' and 'X2', which have major peaks at 2θ angles 6.04° (interplanar spacing d = 6.56 Å) and 2.84° (13.94 Å) respectively. Below the region containing Pd, $PdCl_2$, 'X1' and 'X2', there is another region (points 73-85) containing Pd, CuCl and two other unknown phases 'X3' and 'X4'. 'X3' has major peaks at 5.98° (6.62 Å) and 8.28° (4.79 Å). 'X4' has major peaks at 3.81° (10.38 Å) and 6.23° (6.36 Å). It appears that these are four separate phases because all the peaks attributed to each individual phase

increase and decrease together independently from other phases from point to point (see Supporting Information).

Three other artificial pits were grown at 1.3 V in 0.9% NaCl with additions of 4% albumin, 0.1% H_2O_2 or 4% albumin + 0.1% H_2O_2. In all three electrolytes, diffraction patterns (not shown here) were similar to the ones in Figure 1b and c indicating that additions of albumin or/and H_2O_2 do not significantly influence the nature of the corrosion products. A summary of the crystalline phases found with in situ XRD is given in Table 1.

2.1.2. Corrosion products at lower potentials

One artificial pit was initially grown at 0.7 V, then at 0.5 V and finally at 0 V. XRD patterns were collected in situ at each of the three potentials. Table 1 shows standard crystalline phases matching measured diffraction patterns. Figure 2 shows three diffraction pattern stacks obtained at each of the three potentials. It can be seen in Figure 2, that at 0.7 V Pd appears to be the predominant phase (as it is at 1.3 V) with CuCl close to the interface and two additional unknown phases (see region y = 4.41-4.53 mm in Figure 2b). These appear to be similar to two of the phases at 1.3 V, i.e. ‘X3’ and ‘X4’ (see Figure S4 in Supporting Information).

As Figure 2c shows, diffraction peaks of Pd are present in all measurement locations in the corrosion products at 0.5 V, including close to the interface. Close to the interface the most intense Pd peak (111) is not clearly distinguishable from the main scattering halo of the metallic glass. However, other Pd reflections, e.g. 022 and 113, are clearly visible (not shown here) indicating that Pd is also present in that region. A few patterns consistent with $ZrOCl_2 \cdot 8H_2O$ were found at 0.5 V at a distance of ~70 µm above the interface (see Figure 3a). [14]

Figure 4 shows the evolution of current density with time at 0.7, 0.5 and 0 V corresponding to the diffraction data shown in Figure 2. At 0.7 and 0.5 V, the measured net current density is positive. This is attributed to high anodic dissolution. At 0 V, the current density is initially

high suggesting that the pit remains active i.e. the alloy is dissolving. However, after ~300 s, the current density decays and reaches a relatively steady negative current at 800 s. This is consistent with the pit repassivating (growing an oxide film on the surface) leaving only a small net cathodic current which may be associated with water reduction to form hydrogen and/or reduction of other species in the pit cavity electrolyte, e.g. Cu ions. As indicated by the two blue arrows, most of the diffraction scan shown in Figure 2d was recorded when the current density was negative.

Figure 3b shows a stack of diffraction patterns at 0 V close to the interface. It can be seen that points 1 to 24 show peaks associated with Pd reflections 111, 002, 022 and 113, suggesting the presence of Pd close to the interface. The lattice parameter of Pd close to the interface, e.g. 3.908(5) Å, is larger than that of standard Pd, i.e. 3.89 Å.[15] This is 3.932(1) and 3.9417(3) Å at distances 0.21 and 0.42 mm from the interface, respectively. At 0 V, close to the interface, diffraction peaks matching those of standard Cu_2O were found indicating Cu_2O might form at the interface (see Figure 3b and Figure 2d).[16] As shown in Figure 3b, also close to the interface, in the same region with Cu_2O, there are additional minor peaks, which are attributed to two unknown phases ‘X5’ and ‘X6’. ‘X5’ has major peaks at 5.10° (interplanar spacing d = 7.76 Å) and 10.20° (3.88 Å). ‘X6’ has major peaks at 7.26° (5.45 Å) and 14.37° (2.76 Å). It appears that these are two separate phases because all the peaks attributed to each individual phase increase and decrease together from point to point independently from other phases (see Supporting Information).

The CuCl layer appears to be thicker at lower potentials, i.e. 40 μm at 1.3 V (see Figure 1c), 100 μm at 0.7 V, 300 μm at 0.5 V and 330 μm at 0 V (see Figure 2b-d). The advance of the interface during the time taken to scan through this layer was taken into consideration when calculating the thickness.

Faint diffraction peaks consistent with the presence of Cu crystallites were found at 0.5 V (diffraction peaks not clearly visible in Figure 2c). These were more intense and clearly

visible at 0 V (see Figure 2d). At 0 V, Cu peaks are seen throughout the CuCl layer except for very close to the interface (see Figure 3b). The intensity of the Cu peaks tends to increase with distance from the interface up to ~330 µm while the intensity of the CuCl peaks appears constant.

2.1.3. Influence of electrolyte and potential on lattice parameter and crystallite size of Pd particles

The lattice parameter of Pd was determined for each individual diffraction pattern. Average values for each test condition are given in Table 2. As can be seen in Table 2, in all test conditions except in 0.9% NaCl at 0 V, the lattice parameter of Pd is very similar to that of standard bulk Pd. However, at 0 V this is significantly larger, i.e. 3.908(5) Å close to the interface, increasing to 3.932(1) and further to 3.9417(3) Å at 0.21 and 0.42 mm from the interface.

Figure 3c shows the stack of XRD patterns at 0 V in a selected 2θ region 27-36°. It can be seen that the peaks attributed to Pd 022, 331 and 222 reflections appear at lower 2θ values compared to standard Pd, with peak positions between those of α- and β-PdH_x. Experimental errors can be excluded as other peaks associated with CuCl appear at their standard 2θ positions. Diffraction patterns at higher levels were not collected.

As can be seen in Table 1, albumin does not appear to affect the crystallite size of Pd particles. Peroxide and lower potentials appear to cause a slight decrease in particle size.

It can also be seen in Figure 3c that the Pd peak height shows less variation from pattern to pattern than at higher potentials (compare to Figure 1b) indicating that the corrosion product layer at 0 V may be more compact and uniform.

2.1.4. Unidentified crystalline phases

As mentioned above, the presence of a series of unindexed Bragg peaks indicates that there are additional unidentified crystalline phases, i.e. ‘X1’ to ‘X6’ in Table 1, Figure 1c and

Figure 3b. After analysis, none of the following crystalline phases appear to satisfactorily match those peaks: TiO_2 anatase/rutile/brookite, Ti_2O_3, $TiCl_3$, $H_2Ti_6O_{13}$, ZrO_2, $ZrOCl_2{\cdot}6H_2O$, $CuCl_2$, $CuCl_2{\cdot}2H_2O$, CuO, Cu_3TiO_4 and $SnCl_2$ (a comparison between the diffraction patterns of 'X1'-'X6' and selected standard patterns of some of the mentioned phases is shown in Supporting Information, Figure S4)

2.2. Ex situ characterization of corrosion products with TEM

Figure 5a shows a TEM image of corrosion products generated inside an artificial pit on a $Ti_{40}Zr_{10}Cu_{34}Pd_{14}Sn_2$ metallic glass ribbon in 0.9% NaCl grown at 1.3 V for 4 h to a depth of ~1 mm. Prior to the TEM analysis the corrosion products were immersed in distilled water for 20 h. Therefore, only components which are not soluble in water are present. The observed corrosion products have a particle size of 7 ± 3 nm (range 3-12 nm). EDX analysis indicates these particles consist mostly of Pd and also contain trace levels of Ti, Zr, Cu and Sn (Table 3). Figure 5b shows a TEM image of corrosion products generated at 0.7 V. The particle size is larger than at 1.3 V, i.e. 16 ± 10 nm (range 4-40 nm). EDX analysis indicates that at 0.7 V particles contain less Pd and more Cu than at 1.3 V (Table 3).

Figure 5c shows an electron diffraction pattern measured on corrosion products at 0.7 V. The diffraction pattern is consistent with that of standard Pd except it appears shifted to higher $1/d$ values. A few reasons may contribute to this, e.g. positioning of the sample within the TEM column at a height different from the calibrated one. Similar electron diffraction patterns were obtained for corrosion products at 1.3 V (not shown here).

3. Discussion

It was shown that the $Ti_{40}Zr_{10}Cu_{34}Pd_{14}Sn_2$ metallic glass generates abundant quantities of black corrosion products in artificial pits in 0.9% NaCl with or without additions of 4%

albumin or/and 0.1% H_2O_2 (see Figure 1a). These consist mostly of Pd nanoparticles and include $PdCl_2$, CuCl and other minority phases closer to the dissolving interface.

3.1. Pd nanoparticles

The formation of Pd nanoparticles was clearly demonstrated by in situ XRD (Figure 1b, 1c, 2 and 3b) and ex situ electron diffraction (Figure 5) and EDX (Table 3). They are found throughout the pit cavity from the dissolving interface to the top of the corrosion product layer. Continuous uniform diffraction rings indicate they have a random crystallographic orientation (see Figure S1 in Supporting Information).

The Pd nanoparticles may contain significant amounts of the other alloying elements, i.e. Ti, Zr, Cu, and Sn. As EDX results shown in Table 3 indicate, the Pd particles contain up to 20 at. % of the other alloying elements. However, the lattice parameter of the Pd nanoparticles is very close to that of standard pure Pd (see Table 2). The unaffected Pd lattice parameter is explained by the opposing effects of the other elements. Ti and Cu decrease the lattice parameter of binary Pd solid solutions.[17] Zr and Sn increase it.[18]

The crystallite size of the Pd nanoparticles generated at 1.3 V in 0.9% NaCl calculated with Scherrer formula is 6.8 ± 0.9 nm (see Table 2). This is similar to the size of the Pd nanoparticles measured by TEM, i.e. 7 ± 3 nm (see Figure 5a). This suggests that at 1.3 V Pd nanoparticles consist of single crystallites. At 0.7 V the calculated crystallite size is 3.4 ± 0.4 nm (see Table 2), while the particle size is 16 ± 10 nm (see Figure 5b) suggesting Pd nanoparticles consist of several crystallites.

The formation of crystalline Pd nanoparticles in artificial pits on $Ti_{40}Zr_{10}Cu_{34}Pd_{14}Sn_2$ metallic glass could be explained by a dealloying process as a consequence of the large difference in the equilibrium potentials of Pd and the rest of the alloy components. This is supported by the observation of Pd diffraction peaks immediately above the dissolving interface. The fact that

the Pd particles retain some of the less noble alloy components is also suggestive of a dealloying process.[19]

Generally, dealloying of homogeneous crystalline or amorphous alloys consists of selective dissolution of one or more alloy components and reorganization of the remaining component(s) into a three-dimensional network.[19a] In crystalline alloys, this network often maintains the grain size of the precursor alloy. In amorphous alloys (metallic glasses) this network is an aggregate of nano-crystallites formed during dealloying. This was clearly shown for a series of amorphous alloys.[20] For example, dealloying of $Pd_{80-x}Ni_xP_{20}$ (x = 40, 60 and 70) leads to the formation of a three-dimensional network of Pd with a grain size in the range of 10 nm (size estimated from reported TEM images).[20b] For $Pd_{10}Ni_{70}P_{20}$ the Pd network is very porous, but still continuous. However, in the present study of artificial pits on $Ti_{40}Zr_{10}Cu_{34}Pd_{14}Sn_2$ metallic glass Pd particles are formed instead of a Pd continuous network. It has been noted before that if the concentration of the remaining component is too low, this will fall apart as a suspension of nanoparticles (<20% Au in Au-Ag alloys).[21] Therefore, one reason for the formation of Pd nanoparticles instead of a continuous network is likely to be its relatively low concentration, i.e. 14 at. %.

Experimental evidence and simulations suggest that the intrinsic length scale of dealloyed materials (ligament/pore diameter) is controlled by the rate of dissolution of the less-noble component(s) relative to the rate of reorganization of the noble component(s).[19a, 22] The higher the dissolution rate relative to the reorganization rate, the smaller the length scale. One might envisage that at one extreme, the length scale might be so small that the formation of a continuous network is precluded and instead particles form. Indeed, the dissolution rate in artificial pits on the $Ti_{40}Zr_{10}Cu_{34}Pd_{14}Sn_2$ metallic glass determined in this work is quite high, e.g. ~50 nm s^{-1} at 1.3 V. However, an opposing effect might be caused by a high Cl^- concentration inside the artificial pit,[23] e.g. [Cl^-] >11 M in artificial pits on stainless steels.[24] Adsorption of chloride ions increases the surface diffusion rate,[23] and indeed the Pd ligament

size is larger in the presence of chloride compared to other anions when dealloying Al-Pd alloys.[25]

3.2. Pd nanoparticles at lower potentials

Formation of Pd nanoparticles at 1.3 and 0.7 V has been clearly demonstrated. However, it is not clear whether Pd nanoparticles are generated at 0.5 and 0 V (see Section 2.1.2). Although the metallic glass appears to continue corroding at 0 V, possibly generating new Pd nanoparticles, most of the Pd nanoparticles present in the pit cavity at 0 V were generated at higher potentials. These appear to undergo changes as in situ XRD revealed an increase in their lattice parameter (Figure 3c and Table 2). The lattice parameter of the Pd nanoparticles at 0 V, i.e. 3.908(5) Å close to the interface, increasing to 3.932(1) and further to 3.9417(3) Å at 0.21 and 0.42 mm from the interface, is significantly larger than that of standard Pd seen at higher potentials, i.e. 3.891(5), 3.887(5) and 3.897(3) Å for 1.3, 0.7 and 0.5 V, respectively (see Table 2). The larger lattice parameter could be explained by the formation of substitutional solid solutions of Pd with Zr or Sn or absorption of H. Solid solutions of Pd with either Ti or Cu have lower lattice parameters than pure Pd.[17-18] The solubility of both Zr and Sn in Pd is sufficient to explain the observed lattice parameter values.[18] However, Zr and Sn are not expected to be generated in metallic form and diffuse into Pd nanoparticles away from the interface.

The increase in the lattice parameter of the Pd nanoparticles at 0 V might be explained by absorption of H generated by cathodic reduction of water. Pd forms two distinct hydrides PdH_x, α with $x \leq 0.015$ and β with $0.5 \leq x \leq 0.75$, separated by a miscibility gap, which narrows to some extent in nanoparticles.[26] Both α and β have the crystalline structure of Pd (fcc). For bulk PdH_x, the maximum lattice parameter of the α phase and the minimum one of the β phase (denoted as $a(\alpha_{max})$ and $a(\beta_{min})$) are 3.90 and 4.04 Å, respectively.[27] For 3 nm

PdH_x nanoparticles, $a(\alpha_{max})$ and $a(\beta_{min})$) are 3.91 and 3.97 Å, respectively (Table 2).[28] Peak positions for these values of the lattice parameter (scattering by H was neglected) are shown in Figure 3c. The values observed in this work, i.e. 3.908(5) Å at the interface up to 3.9417(3) Å at 0.42 mm from the interface (Table 2), fall in the miscibility gap indicating the presence of both α- and β-PdH_x. The individual diffraction peaks of the two hydrides could not be resolved. Peak convolution is due to Scherrer broadening and narrowing miscibility gap with decreasing particle size.[26-28] Similarly, Ingham et al. noted the individual diffraction peaks could not be resolved for particle size 3 nm or lower.[28]

As mentioned, the Pd nanoparticle layer at 0 V appears to be quite compact. This indicated that the particles could be in electrical contact among themselves and with the metallic glass surface, thus providing the necessary path for electrons to travel to the H reduction site on the particles. As shown in Figure 4, the measured net current is negative indicating a significant cathodic reaction, which could be attributed to H reduction on the Pd nanoparticles.

3.3. $PdCl_2$

A layer of the corrosion products at 1.3 V in 0.9% NaCl (+ 4% albumin, + 0.1% H_2O_2, + 4% albumin + 0.1% H_2O_2) originates diffraction patterns similar to a pattern of commercially sourced $PdCl_2$ (unknown preparation method) reported by Hanawalt et al. in 1938 (see Figure 1c and Table 1).[29] It was indexed as an orthorhombic crystal structure, space group *Pnnm*, but the structure was not fully solved. Over time, four polymorphs have been reported for $PdCl_2$, including a glassy state.[30] Among the four polymorphs, the one stable at room temperature, γ-$PdCl_2$ has a diffraction pattern closest to the one reported by Hanawalt et al. and those reported by the present work.[30b] γ-$PdCl_2$ has a monoclinic structure (space group $P2_1/c$) with two formula units in the unit cell.[30b]

It was reported that electrochemical dissolution of powdered Pd from graphite anodes in HCl solution generates $PdCl_2$.[30c, 31] However, it was not mentioned which polymorph of $PdCl_2$ formed.

$PdCl_2$ is insoluble in water while in concentrated HCl solutions Pd is present as the complex ion $[PdCl_4]^{2-}$.[30c] In this work $PdCl_2$ was detected starting at a distance of 100 µm from the dissolving interface. This suggests that at the dissolving interface, where the solution concentration is close to saturation, and the chloride concentration and acidity are high, some Pd may dissolve in the form of $[PdCl_4]^{2-}$, but as the complex ion diffuses away from the interface to where the water activity is higher, then $PdCl_2$ is able to nucleate.

3.4. CuCl

CuCl was found in all test conditions immediately above the dissolving interface (see Figure 1c and 2, and Table 1). The thickness of the CuCl is larger at lower potentials (see Results).

Using ex situ methods, CuCl was found at the bottom of regular and artificial pits on pure Cu in (artificial) drinking water.[32] Ex situ XPS indicated the formation of CuCl on the surface of Cu polarised in NaCl electrolytes.[33] CuCl was also found with in situ grazing incidence XRD in pits on Cu grown in 0.1 N NaCl, pH 12.[34] CuCl has a zinc-blende structure, space group *F*-43*m*.[35]

3.5. Metallic Cu at lower potentials

Cu particles might be generated at lower potentials. In situ XRD revealed traces of Cu at 0.5 V and more significant quantities at 0 V (see Figure 2 and Table 1). At 0 V, Cu appears to be present throughout the CuCl layer, and the amount of Cu appears to increase with distance from interface (see Figure 2d) indicating that formation of Cu might be related to the CuCl. The possibility of Cu formation by dealloying can be excluded since there is no clear sign of

Cu immediately above the interface. Instead it may be suggested that Cu is plated on existing Pd nanoparticles by reduction of existing CuCl, i.e. $CuCl + e^- \rightleftharpoons Cu + Cl^-$.[36] As explained earlier for the case of H, the Pd particles might be in electrical contact, thus ensuring a path for electrons to travel to the site of CuCl reduction.

The formation of Cu particles may also be caused by X-ray beam damage effects. Mesu et al. revealed the formation of colloidal Cu nanoparticles in $CuCl_2$ aqueous solutions when irradiated with X-rays.[37] CuCl is also susceptible to photochemical disproportionation into Cu^0 and Cu^{2+} in the presence of H_2O.[38] The artificial pits in this work were illuminated constantly for imaging purposes. In this case, the dependence of Cu quantity on distance from interface would be explained by the exposure time, i.e. CuCl at higher levels has been generated earlier and therefore was exposed for longer time to ambient light.

3.6. Other phases

Traces of $ZrOCl_2 \cdot 8H_2O$ were detected at 0.5 V in 0.9% NaCl. This is consistent with our recent finding that $ZrOCl_2 \cdot 8H_2O$ is generated in artificial pits on pure Zr in 0.9% NaCl.[39] Cu_2O appears to form at 0 V close to the interface (Figure 2 and Figure 3b). Cu_2O is stable in neutral and alkaline media and might have formed by oxidation of Cu in the metallic glass or hydrolysis of CuCl in either case indicating an increase in pH. As Figure 4 shows at the beginning of the diffraction scan at 0 V, the pit appears to repassivate, in which case anodic dissolution stops, ions diffuse away and water diffuses towards the interface. Reduction of water takes place, which increases the pH and increases the stability of Cu_2O.

It is not clear what are the unidentified phases found especially at high potentials, i.e. ‘X1’ to ’X4’. They exhibit Bragg peaks at low diffraction angles indicating they have large unit cells. They are possibly complex oxychlorides given the multi-element alloy composition and the highly acidic, high chloride concentration pit environment. As mentioned above, close analysis suggests these are not any of a number of expected compounds like TiO_2, $CuCl_2$ or

$CuCl_2 \cdot 2H_2O$. In any case, these unidentified compounds are reported to be soluble due to the concentration observed.

Ti is the most abundant element of the metallic glass and would be expected to generate abundant quantities of corrosion products inside or/and outside the artificial pit. In situ XRD inside the artificial pits gave no clear indication of crystalline Ti compounds in any test condition, e.g. Ti oxides, $TiCl_3$ (four different polymorphs of $TiCl_3$ have been reported previously).[40] Furthermore, TEM/EDX analysis revealed a limited concentration of Ti, i.e. 5 at. % (see Table 3). These may suggest most of the corroded Ti is located in the corrosion products outside the artificial pits. However, these were not interrogated.

Previous work on characterisation of corrosion products of Ti in artificial pits is scarce. Beck observed white precipitate at the outer part of artificial pits on Ti and assumed it to be TiO_2.[41] He proposed as pathway the formation of $TiCl_4$ at the dissolving interface followed by hydrolysis to TiO_2. In situ X-ray absorption near edge structure (XANES) measurements on artificial pits on pure Ti indicated the generation of crystalline Ti oxides rutile and anatase, $TiCl_4$ and metallic Ti fragments.[11] However, this study did not consider amorphous TiO_2. Additionally, several studies have shown that diluting $TiCl_4$ in H_2O leads to formation of amorphous TiO_2 nanoparticles.[42] In consequence, it could be expected for artificial pits on the $Ti_{40}Zr_{10}Cu_{34}Pd_{14}Sn_2$ metallic glass that Ti leads to the formation of $TiCl_4$ and hydrolysis of $TiCl_4$ (liquid at room temperature) in turn leads to rutile, anatase and/or amorphous TiO_2. These would be difficult to pick up by XRD due to their low concentrations inside the pits, i.e. 5 at. % Ti measured ex-situ by TEM/EDX, and due to the lack of long-range order of amorphous TiO_2. Nevertheless, most of the corroded Ti could be located in the corrosion products outside the artificial pits (not analysed in this work) in agreement with the observation of Beck for pure Ti electrodes.[41]

3.7. Influence of albumin or/and H_2O_2 additions and applied potential on corrosion products

Additions of 4% albumin, 0.1% H_2O_2 or 4% albumin + 0.1% H_2O_2 do not appear to change significantly the nature and the layout of the corrosion products generated in artificial pits on the $Ti_{40}Zr_{10}Cu_{34}Pd_{14}Sn_2$ metallic glass in 0.9% NaCl (see Table 1). However, the applied potential has a significant effect. Pd nanoparticles clearly form at high potentials 1.3 and 0.7 V and might also form at lower potentials (Figure 1b and Figure 2). The Pd particle size appears to increase with decreasing potential while the crystallite size decreases (Figure 5 and Table 2). The Pd nanoparticles contain other elements (Ti, Zr Cu and Sn) and the Cu content appears to increase with decreasing potential (Table 3). Pd hydride might form at lower potentials. $PdCl_2$ is generated only at sufficiently high potentials, e.g. at 1.3 V, but not at or below 0.7 V (Figure 1c and Table 1). CuCl is generated at all potentials and its abundance increases with decreasing potential (Figure 1b and Figure 2). CuCl appears to be accompanied by an unidentified crystalline phase ('X4') at all potentials except the lowest, i.e. 0 V. Cu and Cu_2O might be generated at lower potentials. Several other minority compounds form at higher potentials, which could not be identified (see Table 1).

3.8. Implications

$Ti_{40}Zr_{10}Cu_{34}Pd_{14}Sn_2$ metallic glass shows good corrosion resistance with a broad passive region and relatively high pitting potential so they are not expected to corrode in normal physiological conditions. However, if they are vulnerable to local processes such as MACC, they may generate corrosion products similar to the ones found in this work. It is therefore appropriate to consider the biological significance of the species found in this study. Pd nanoparticle exposures has been studied in both in vitro and in vivo studies.[43] In cell culture, Pd nanoparticles have variable effects on cell growth and viability, dependent on cell type and nanoparticle size and exposure concentration.[43a] Immuno-modulatory effects of Pd

nanoparticles have been reported following exposures on peripheral blood mononuclear cells from both Pd-sensitized and non-atopic subjects,[44] however in in vivo studies the impact of Pd nanoparticle exposure on immune function is not clear.[43a] In contrast to Pd, Cu is an element of importance for a range of physiological processes including angiogenesis and cellular energy production. However, high concentration exposures of Cu ions and Cu oxide particles can induce cellular toxicity.[45] The impact of the corrosion products identified in this study on peri-implant tissues and immune cell function requires further investigation, however, the conditions in which they were generated only approximate the physiological environment. Firstly, the electrolyte used in this study, i.e. 0.9 M NaCl, is a simple simulated body environment solution routinely used to determine the general corrosion behavior of implant devices.[46] The in vivo corrosion environment is much more complex containing various inorganic and organic components which may influence the corrosion behavior of implant surfaces. Proteins and reactive oxygen species play an important role in determining the corrosion process.[12, 46] However, it was shown in this study that those components do not appear to significantly change the nature of the corrosion products in artificial pits on the $Ti_{40}Zr_{10}Cu_{34}Pd_{14}Sn_2$ metallic glass. Secondly, the artificial pits in this study were grown at various potentials in the interval 0 to 1.3 V and it was seen that the potential has a significant effect on the nature of the corrosion products. In vivo potentials are virtually impossible to measure, but laboratory corrosion experiments in simulated body conditions indicate values to be in the interval -0.15 to 0.1 V.[2b, 7] Therefore, if corrosion products formed in vivo, these should resemble more the corrosion products in this study at 0 V including Pd hydride, CuCl, Cu_2O and possibly metallic Cu. Finally, due to practical considerations, all the tests in this study have been carried out at room temperature, i.e. 23 ± 1°C. Similar corrosion products may be expected at body temperature, i.e. 37°C, as this is comparable to the test temperature.

4. Conclusion

Artificial pits were grown in a $Ti_{40}Zr_{10}Cu_{34}Pd_{14}Sn_2$ metallic glass in 0.9% NaCl (+ 4% albumin, + 0.1% H_2O_2, + 4% albumin + 0.1% H_2O_2) at 1.3 V vs. Ag/AgCl as well as in 0.9% NaCl at 0.7, 0.5 and 0 V. Corrosion products inside artificial pits were investigated in situ with synchrotron XRD.

In all cases, the pit cavity contains a black layer, predominantly Pd nanoparticles, and closer to the interface CuCl. In and above the CuCl layer, there are additional crystalline phases. Pd nanoparticles contain significant amounts of other alloying elements and their size is 7 ± 3 and 16 ± 10 nm at 1.3 and 0.7 V respectively. Pd hydride might form at the lowest potential, 0 V, following repassivation of the pit. CuCl is more abundant at lower potentials.

$PdCl_2$ was found at 1.3 V. Metallic Cu was observed at 0 V and in trace amounts at 0.5 V. Small amounts of $ZrOCl_2{\cdot}8H_2O$ and Cu_2O were found at 0.5 V and 0 V respectively. Additional minority unidentified crystalline compounds with large unit cells were detected at and above 0.5 V. No indication of any crystalline Ti compounds was found.

Additions of 4% albumin or/and 0.1% H_2O_2 do not alter significantly the nature of the crystalline corrosion products at 1.3 V.

5. Experimental Section

Materials and Electrolytes: Ingots with the nominal composition $Ti_{40}Zr_{10}Cu_{34}Pd_{14}Sn_2$ (at. %) were prepared by arc melting in a Ti-gettered Ar atmosphere (99.999%) starting from pure elements. In order to achieve a homogenous chemical composition, the ingot was melted three times and this was flipped before each re-melting. Chemical analysis by inductively coupled plasma optical emission spectroscopy (ICP-OES) resulted in: 40.9 at% Ti, 10.2 at% Zr, 34.4 at% Cu, 12.5 at% Pd and 2.0 at% Sn. From those ingots, ribbons were prepared by melt-spinning on a Cu wheel at 32 m s^{-1} tangential speed in Ar atmosphere (99.999%, 350 mbar). For melt-spinning, melting was done by induction heating in graphite crucibles. The width and the thickness of the final ribbon varied along the ribbon in the intervals 0.85-3.49 mm and

0.05-0.12 mm. The amorphous structure of the ribbons was confirmed by X-ray diffraction (not shown here).

Electrolytes were prepared from NaCl, albumin (≥98%), H_2O_2 (30% w/v) (all three from Sigma Aldrich, UK), and deionized water (resistivity 18 MΩ·cm, Millipore, UK).

Electrochemical Experiments: Artificial pit experiments were carried out using a three-electrode electrochemical cell described previously.[47] The working electrode consisted of $Ti_{40}Zr_{10}Cu_{34}Pd_{14}Sn_2$ metallic glass ribbons approximately 1 cm long and embedded in non-crystalline Araldite epoxy resin (3M) such that only the cross section was exposed to the electrolyte. The embedded ribbon was attached with non-crystalline Kapton tape (3M) at the bottom side of a plastic cell containing electrolyte (~20 mL). An artificial pit was formed by dissolving the ribbon to a depth of at least 0.5 mm. The reference electrode was Ag/AgCl, 3 M NaCl (E = 0.209 V vs. SHE) and the counter electrode was a platinum wire. All potential values in this paper are relative to the equilibrium potential of Ag/AgCl, 3 M NaCl, unless otherwise stated. Experiments were performed in four different electrolytes, i.e. 0.9% NaCl (+ 4% albumin, + 0.1% H_2O_2, + 4% albumin + 0.1% H_2O_2). Potentiostatic and cyclic potential sweep tests were carried out with two potentiostats: Ivium CompactStat (IVIUM Technologies, Netherlands) and ACM (ACM Instruments, UK). The artificial pits were monitored with a digital optical microscope.

In situ synchrotron XRD experiments: In-situ synchrotron X-ray diffraction (XRD) experiments were carried out at Diamond Light Source, beamline I18 with a focal spot size of 3 μm (v) x 10 μm (h) and beam energy of 17950 eV (0.6907 Å).[48] Diffraction patterns were recorded using a sCMOS detector with pixel size 26 μm x 26 μm (Photonic Science 4k x 2k pixel detector). The detector exposure time for each diffraction image was 10, 20 or 30 s. Artificial pit cells described above were mounted on a precision positioning stage on the beamline. In order to collect series of diffraction patterns of corrosion products at various relative distances to the corroding metal surface and into the metal, the stage was raised

stepwise automatically with a constant predefined step size in the interval 3-200 µm. Detector calibration and azimuthal integration of raw two-dimensional diffraction patterns were performed with the software DAWN.[49] Crystallite sizes were determined with Scherrer formula.[13] Instrumental broadening was assumed to have a value of 0.1°

In situ synchrotron XRD experiments were carried out on artificial pits grown at 1.3 V in 0.9% NaCl (+ 4% albumin, + 0.1% H_2O_2, + 4% albumin + 0.1% H_2O_2). One individual artificial pit was used for each of the four electrolytes. One additional artificial pit was grown in 0.9% NaCl, initially at 0.7 V and subsequently at 0.5 and 0 V. When stepping down the potential, the corrosion products were not removed. Therefore, the pit cavity at the lower potentials contains corrosion products generated at higher potentials.

Ex situ TEM investigations: Artificial pits were grown in 0.9% NaCl at 1.3 and 0.7 V. Immediately after the polarization was stopped, the bulk electrolyte was removed and the pit electrolyte containing the corrosion products were extracted with a micropipette and diluted in de-ionized water. After the corrosion products settled, these were transferred with a micropipette onto a TEM grit. TEM investigations were carried out by means of a Talos microscope (FEI) at an acceleration voltage of 200 kV.

Statistical analysis: Lattice parameter values are presented as mean values with the first non-zero figure of the standard deviation given in brackets (the decimal position of this figure is the same as the last given decimal of the mean). Crystallite size and concentration values are presented as mean ± standard deviation. The sample size (*n*) for each reported value is given in Tables 2 and 3. The mean and the standard deviation values were calculated with Microsoft Excel 2016.

Supporting Information

Supporting Information is available from the Wiley Online Library or from the author.

Acknowledgements

The authors thank Gareth Douglas for preliminary TEM work and Tzu-Yu Chen for lab-based XRD. P.F. Gostin acknowledges Mariana Calin and Daniel Reed for fruitful discussions. This project has received funding from the European Union's Horizon 2020 research and innovation programme under the Marie Sklodowska-Curie grant agreement No 659226. We thank Diamond Light Source for access to beamline I18 (proposal SP13963) that contributed to the results presented here.

Received: ((will be filled in by the editorial staff))
Revised: ((will be filled in by the editorial staff))
Published online: ((will be filled in by the editorial staff))

References

[1] A. Pandit, J. Planell, M. Navarro, in *Biomaterials science. An introduction to materials in medicine* (Eds: B. D. Ratner, A. S. Hoffman, F. J. Schoen, J. E. Lemons), Academic Press, Amsterdam **2013**, Ch. I.2.3.
[2] a) M. Calin, A. Gebert, A. C. Ghinea, P. F. Gostin, S. Abdi, C. Mickel, J. Eckert, *Mater. Sci. Eng. C* **2013**, *33*, 875; b) J.-J. Oak, D. V. Louzguine-Luzgin, A. Inoue, *Mater. Sci. Eng. C* **2009**, *29*, 322.
[3] J. L. Gilbert, in *ASM International Handbook*, Vol. 13C (Eds: S. D. Cramer, B. S. J. Covino), ASM International, Materials Park, Ohio **2006**, Ch. Mechanically Assisted Corrosion of Metallic Biomaterials.
[4] S. L. Zhu, X. M. Wang, A. Inoue, *Intermetallics* **2008**, *16*, 1031.
[5] A. Liens, A. Etiemble, P. Rivory, S. Balvay, J.-M. Pelletier, S. Cardinal, D. Fabrègue, H. Kato, P. Steyer, T. Munhoz, J. Adrien, N. Courtois, D. Hartmann, J. Chevalier, *Materials* **2018**, *11*.
[6] R. Kokubun, W. Wang, S. Zhu, G. Xie, S. Ichinose, S. Itoh, K. Takakuda, *Bio-Med. Mater. Eng.* **2015**, *26*, 9.
[7] F. X. Qin, X. M. Wang, S. L. Zhu, A. Kawashima, K. Asami, A. Inoue, *Mater. Trans., JIM* **2007**, *48*, 515.
[8] O. Addison, A. J. Davenport, R. J. Newport, S. Kalra, M. Monir, J. F. Mosselmans, D. Proops, R. A. Martin, *J. R. Soc. Interface* **2012**, *9*, 3161.
[9] ASTM, *F2129-17 Standard Test Method for Conducting Cyclic Potentiodynamic Polarization Measurements to Determine the Corrosion Susceptibility of Small Implant Devices*, ASTM International, **2017**.
[10] J. Srinivasan, M. J. McGrath, R. G. Kelly, *J. Electrochem. Soc.* **2015**, *162*, C725.
[11] M. Monir, *PhD Thesis*, University of Birmingham, September, **2011**.
[12] F. Yu, O. Addison, A. J. Davenport, *Acta Biomater.* **2015**, *26*, 355.
[13] B. D. Cullity, *Elements of x-ray diffraction*, Addison-Wesley Publishing Company, Inc., **1978**.
[14] ICDD Database, *Diffraction data of ZrOCl2·8H2O with reference code 00-032-1498.*
[15] a) ICSD Database, *Diffraction data of Pd with reference code 648675*; b) I. R. Harris, M. Norman, W. E. Gardner, *J. Less-Common Met.* **1972**, *29*, 299.

[16] a) A. Kirfel, K. Eichhorn, *Acta Crystallogr. Sect. A* **1990**, *46*, 271; b) ICSD Database, *Diffraction data of Cu2O with reference code 52043*.
[17] a) J. Evans, I. R. Harris, L. S. Guzei, *J. Less-Common Met.* **1979**, *64*, 39; b) J. O. Linde, *Ann. Phys. (Berlin Ger.)* **1932**, *15*, 249.
[18] a) M. Ellner, *J. Alloys Compd.* **2004**, *366*, 222; b) I. R. Harris, M. Cordey-Hayes, *J. Less-Common Met.* **1968**, *16*, 223.
[19] a) I. McCue, E. Benn, B. Gaskey, J. Erlebacher, *Annu. Rev. Mater. Res.* **2016**, *46*, 263; b) J. Snyder, P. Asanithi, A. B. Dalton, J. Erlebacher, *Adv. Mater.* **2008**, *20*, 4883.
[20] a) F. Scaglione, F. Celegato, P. Rizzi, L. Battezzati, *Intermetallics* **2015**, *66*, 82; b) Y. Q. Zeng, S. C. Yang, H. Xiang, X. Z. Dong, L. Y. Chen, M. W. Chen, A. Inoue, X. H. Zhang, J. Q. Jiang, *Intermetallics* **2015**, *61*, 66; c) J. Yu, Y. Ding, C. Xu, A. Inoue, T. Sakurai, M. Chen, **2008**; d) E. M. Paschalidou, F. Celegato, F. Scaglione, P. Rizzi, L. Battezzati, A. Gebert, S. Oswald, U. Wolff, L. Mihaylov, T. Spassov, *Acta Mater.* **2016**, *119*, 177.
[21] F. Kertis, J. Snyder, L. Govada, S. Khurshid, N. Chayen, J. Erlebacher, *JOM* **2010**, *62*, 50.
[22] J. Erlebacher, M. J. Aziz, A. Karma, N. Dimitrov, K. Sieradzki, *Nature* **2001**, *410*, 450.
[23] R. C. Newman, K. Sieradzki, *Science* **1994**, *263*, 1708.
[24] H. S. Isaacs, J. H. Cho, M. L. Rivers, S. S. R, *J. Electrochem. Soc.* **1995**, *142*, 1111.
[25] Z. H. Zhang, Y. Wang, Z. Qi, W. H. Zhang, J. Y. Qin, J. Frenzel, *J. Phys. Chem. C* **2009**, *113*, 12629.
[26] W. Vogel, W. He, Q.-H. Huang, Z. Zou, X.-G. Zhang, H. Yang, *Int. J. Hydrogen Energy* **2010**, *35*, 8609.
[27] J. A. Eastman, L. J. Thompson, B. J. Kestel, *Phys. Rev. B* **1993**, *48*, 84.
[28] B. Ingham, M. F. Toney, S. C. Hendy, T. Cox, D. D. Fong, J. A. Eastman, P. H. Fuoss, K. J. Stevens, A. Lassesson, S. A. Brown, M. P. Ryan, *Phys. Rev. B* **2008**, *78*.
[29] J. D. Hanawalt, H. W. Rinn, L. K. Frevel, *Ind. Eng. Chem. Anal. Ed.* **1938**, *10*, 0457.
[30] a) D. B. Dell'Amico, F. Calderazzo, F. Marchetti, S. Ramello, *Angew. Chem. Int. Ed.* **1996**, *35*, 1331; b) J. Evers, W. Beck, M. Gobel, S. Jakob, P. Mayer, G. Oehlinger, M. Rotter, T. M. Klapotke, *Angew. Chem. Int. Ed. Engl.* **2010**, *49*, 5677; c) W. P. Griffith, S. D. Robinson, K. Swars, *Pd Palladium: Palladium Compounds*, Springer Berlin Heidelberg, Berlin, Heidelberg **1989**; d) J. R. Soulen, W. H. Chappell Jr., *J. Phys. Chem.* **1965**, *69*, 3669; e) A. F. Wells, *Z. Kristallogr.* **1938**, *100*, 189.
[31] a) A. I. Volfson, A. I. Ryazanov, G. D. Chigrinova, *J. Appl. Chem. (USSR)* **1961**, *34*, 173; b) A. I. Ryazanov, A. I. Volfson, G. D. Chigrinova *USSR Patent 138922* **1959**.
[32] a) M. Pourbaix, *J. Electrochem. Soc.* **1975**, *123*, 25C; b) H. Ha, C. Taxen, K. Williams, J. Scully, *Electrochim. Acta* **2011**, *56*, 6165; c) H. M. Ha, J. R. Scully, *J. Electrochem. Soc.* **2012**, *159*, C571.
[33] A. E. Warraky, H. A. E. Shayeb, E. M. Sherif, *Anti-Corros. Methods Mater.* **2004**, *51*, 52.
[34] S. Sathiyanarayanan, M. Sahre, W. Kautek, *Corros. Sci.* **1999**, *41*, 1899.
[35] S. Hull, D. A. Keen, *Phys. Rev. B* **1994**, *50*, 5868.
[36] J. v. Muylder, N. d. Zoubov, M. Pourbaix, *Diagrammes d'equilibres tension-pH des systemes Cu-H2O et Cu-Cl-H2O*, Report no. 101, CEBELCOR, **1962**. (http://www.cebelcor.org/publications.lasso?Id=1&SubCat=copper%20and%20alloys)
[37] J. G. Mesu, A. M. Beale, F. M. F. de Groot, B. M. Weckhuysen, *J. Phys. Chem.* **2006**, *110*, 17671.
[38] B. Carlsson, G. Wettermark, *J. Photochem.* **1976**, *5*, 321.
[39] Y. Zhang, O. Addison, P. F. Gostin, A. Morrell, A. Cook, A. Liens, J. Wu, K. Ignatyev, M. Stoica, A. Davenport, *J. Electrochem. Soc.* **2017**, *164*, C1003.

[40] a) F. Auriemma, V. Busico, P. Corradini, M. Trifuoggi, *Eur. Polym. J.* **1992**, *28*, 513; b) G. Natta, P. Corradini, G. Allegra, *J. Polym. Sci.* **1961**, *51*, 399.
[41] T. R. Beck, *J. Electrochem. Soc.* **1973**, *120*, 1317.
[42] a) Q. Zhang, L. Gao, J. Guo, *J. Eur. Ceram. Soc.* **2000**, *20*, 2153; b) H. Bao, H. Zhang, G. Liu, Y. Li, W. Cai, *Langmuir* **2017**, *33*, 5430.
[43] a) V. Leso, I. Iavicoli, *Int. J. Mol. Sci.* **2018**, *19*; b) I. Iavicoli, M. Farina, L. Fontana, D. Lucchetti, V. Leso, C. Fanali, V. Cufino, A. Boninsegna, K. Leopold, R. Schindl, D. Brucker, A. Sgambato, *Toxicol. in Vitro* **2017**, *42*, 191.
[44] a) P. Boscolo, V. Bellante, K. Leopold, M. Maier, L. Di Giampaolo, A. Antonucci, I. Iavicoli, L. Tobia, A. Paoletti, M. Montalti, C. Petrarca, N. Qiao, E. Sabbioni, M. Di Gioacchino, *J. Biol. Regul. Homeost. Agents* **2010**, *24*, 207; b) M. Reale, G. Vianale, L. V. Lotti, R. Mariani-Costantini, S. Perconti, A. Cristaudo, K. Leopold, A. Antonucci, L. Di Giampaolo, I. Iavicoli, M. Di Gioacchino, P. Boscolo, *J. Occup. Environ. Med.* **2011**, *53*, 1054.
[45] A. Semisch, J. Ohle, B. Witt, A. Hartwig, *Part. Fibre Toxicol.* **2014**, *11*, 10.
[46] K. J. Bundy, in *Corrosion Tests and Standards: Application and Interpretation* (Ed: R. Baboian), ASTM International, West Conshohocken, PA **2005**, Ch. 42.
[47] T. Rayment, A. J. Davenport, A. J. Dent, J.-P. Tinnes, R. J. K. Wiltshire, C. Martin, G. Clark, P. Quinn, J. F. W. Mosselmans, *Electrochem. Commun.* **2008**, *10*, 855.
[48] J. F. W. Mosselmans, P. D. Quinn, A. J. Dent, S. A. Cavill, S. D. Moreno, A. Peach, P. J. Leicester, S. J. Keylock, S. R. Gregory, K. D. Atkinson, J. R. Rosell, *J. Synchrotron Radiat.* **2009**, *16*, 818.
[49] M. Basham, J. Filik, M. T. Wharmby, P. C. Chang, B. El Kassaby, M. Gerring, J. Aishima, K. Levik, B. C. Pulford, I. Sikharulidze, D. Sneddon, M. Webber, S. S. Dhesi, F. Maccherozzi, O. Svensson, S. Brockhauser, G. Naray, A. W. Ashton, *J. Synchrotron Radiat.* **2015**, *22*, 853.

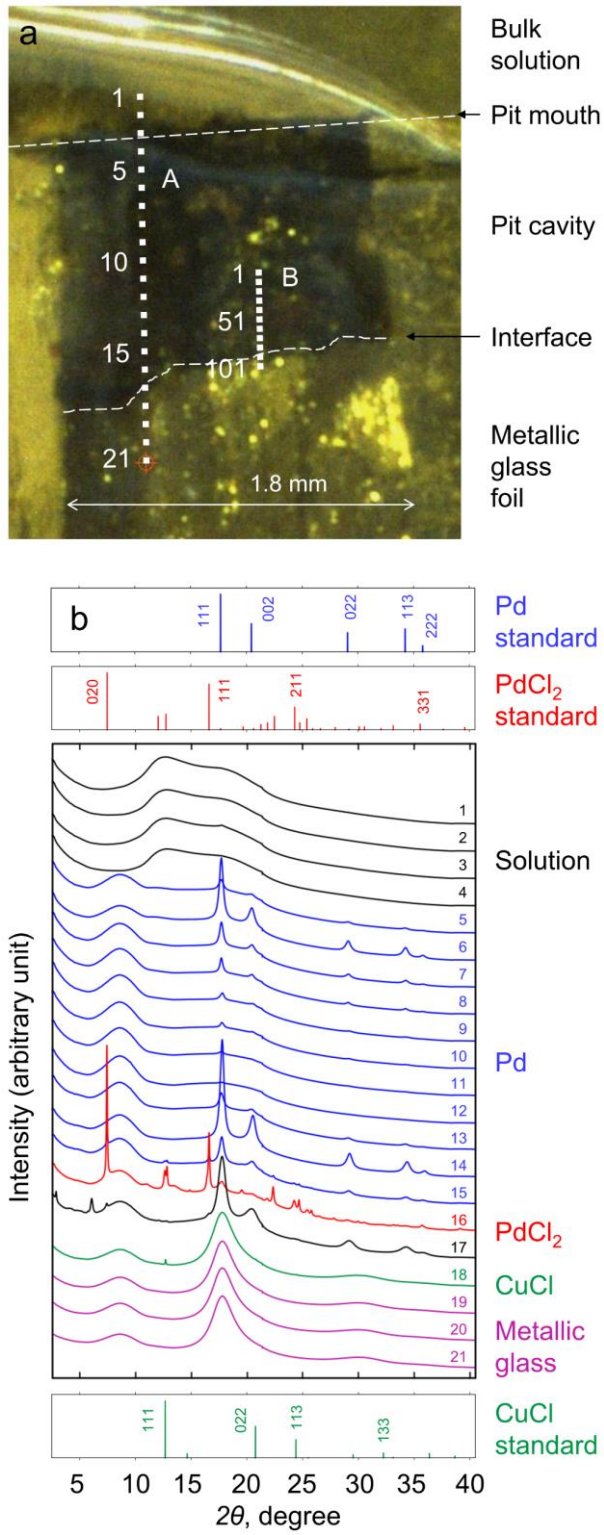

(see next page for Figure 1 part c)

Figure 1. (a) Optical image of a $Ti_{40}Zr_{10}Cu_{34}Pd_{14}Sn_2$ metallic glass artificial pit in 0.9% NaCl at 1.3 V. The lines indicate the approximate location where scans of X-ray diffraction were collected. For scan line 'A', the dots indicate the location where individual diffraction patterns were collected (100 µm spacing). For scan line 'B', the dots indicate every tenth location (5 µm spacing between individual locations). Foil thickness: 90 µm. (b) Stack of X-ray diffraction patterns collected along dotted line 'A'. (c) Stack of X-ray diffraction patterns collected along dotted line 'B'. Every second pattern only is shown here for clarity.

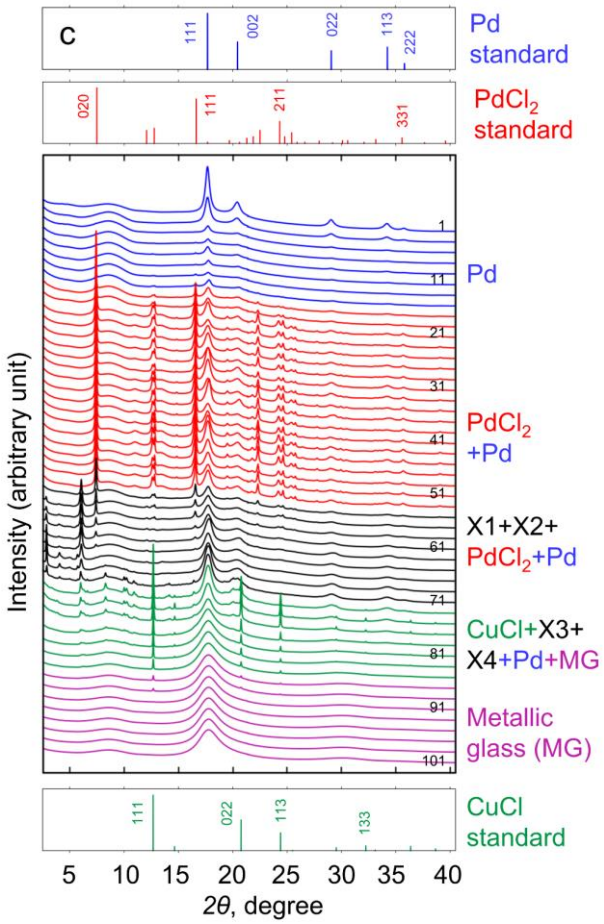

(see previous page for Figure 1 parts a and b)

Figure 1. (a) Optical image of a $Ti_{40}Zr_{10}Cu_{34}Pd_{14}Sn_2$ metallic glass artificial pit in 0.9% NaCl at 1.3 V. The lines indicate the approximate location where scans of X-ray diffraction were collected. For scan line 'A', the dots indicate the location where individual diffraction patterns were collected (100 µm spacing). For scan line 'B', the dots indicate every tenth location (5 µm spacing between individual locations). Foil thickness: 90 µm. (b) Stack of X-ray diffraction patterns collected along dotted line 'A'. (c) Stack of X-ray diffraction patterns collected along dotted line 'B'. Every second pattern only is shown here for clarity.

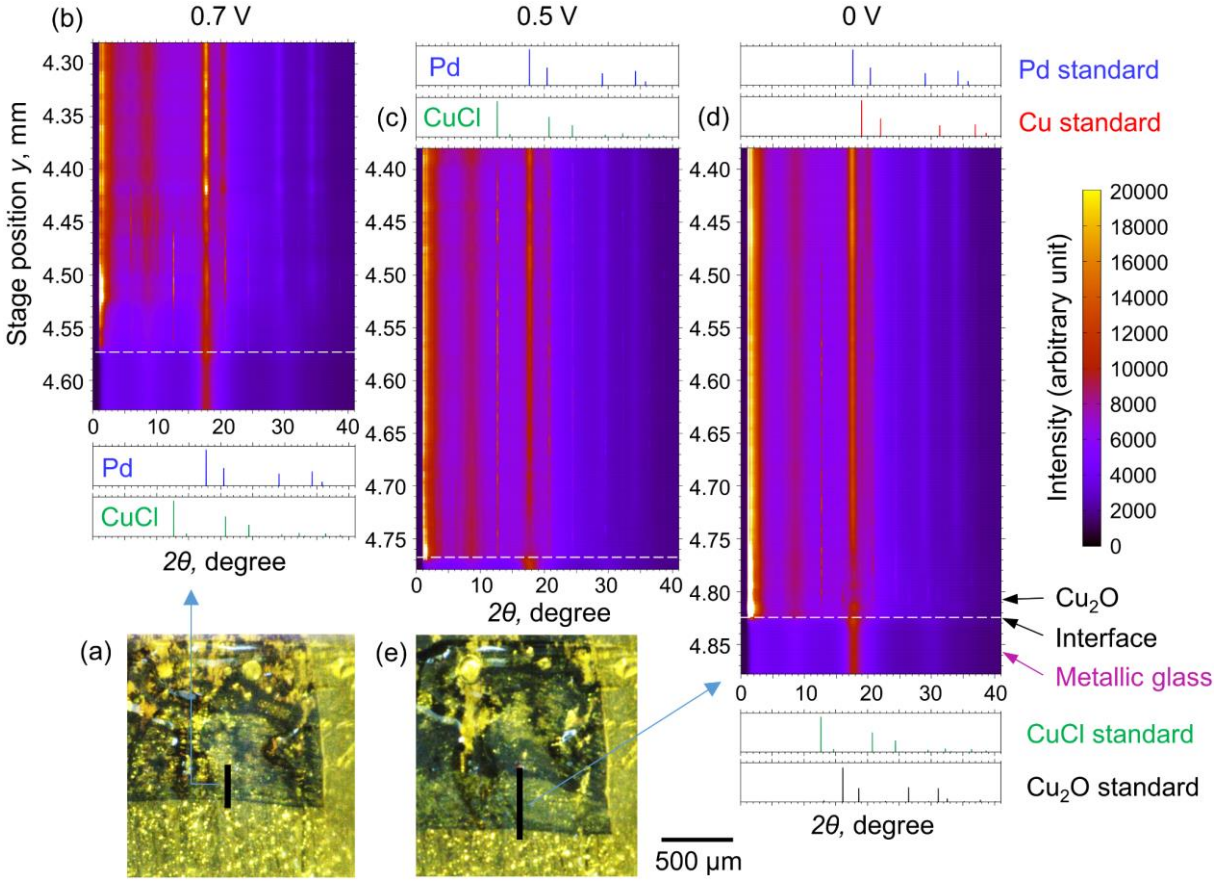

Figure 2. Artificial pit grown on $Ti_{40}Zr_{10}Cu_{34}Pd_{14}Sn_2$ (at. %) metallic glass in 0.9% NaCl first at 0.7, then at 0.5 and finally at 0 V. (a) and (e) are optical images at 0.7 and 0 V. The thick black lines indicate where (approximately) XRD line scans were taken from. (b), (c) and (d) are XRD pattern stacks measured at 0.7, 0.5 and 0 V respectively. The ordinate axes represent the sample stage position where individual patterns were measured. The three diffraction pattern stacks were taken at the same lateral position and are vertically aligned. The colour palette on the right hand side applies to all three stacks. Probing X-ray beam was 3 µm high (10 µm wide) and patterns were collected in 3 µm steps.

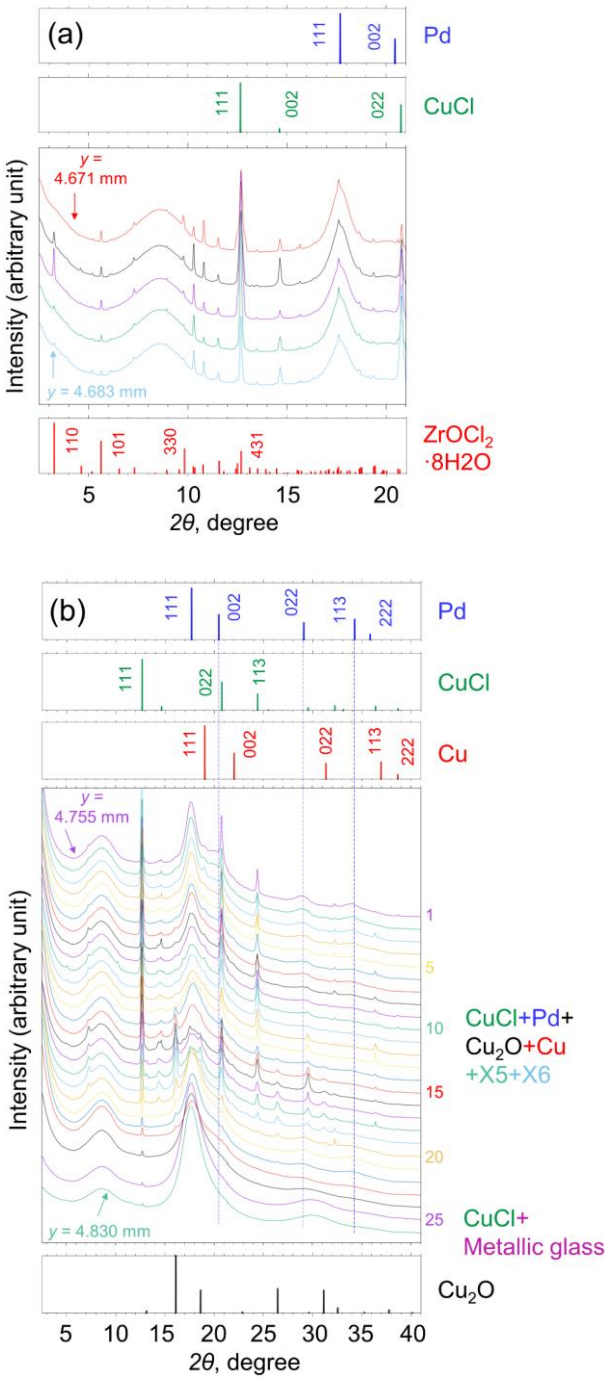

(see next page for Figure 3 part c)

Figure 3. Stacks of X-ray diffraction patterns collected at 3 µm spacing in an artificial pit on $Ti_{40}Zr_{10}Cu_{34}Pd_{14}Sn_2$ metallic glass in 0.9% NaCl: (a) at 0.5 V vs. Ag/AgCl at a distance of ~70 µm above the interface, (b) at 0 V vs. Ag/AgCl close to the interface, the *y* values are in reference to the *y* axis values in Figure 2d, and (c) at 0 V vs. Ag/AgCl from the metallic glass to a distance of ~420 µm from the interface. Also shown, for comparison: standard patterns for Pd, CuCl, Cu, $ZrOCl_2{\cdot}8H_2O$, Cu_2O, and two simulated patterns for Pd with larger lattice parameters (values in legend) to represent PdH_x. The pit depth is ≈1.8 mm. The pit was initially grown at 0.7 V.

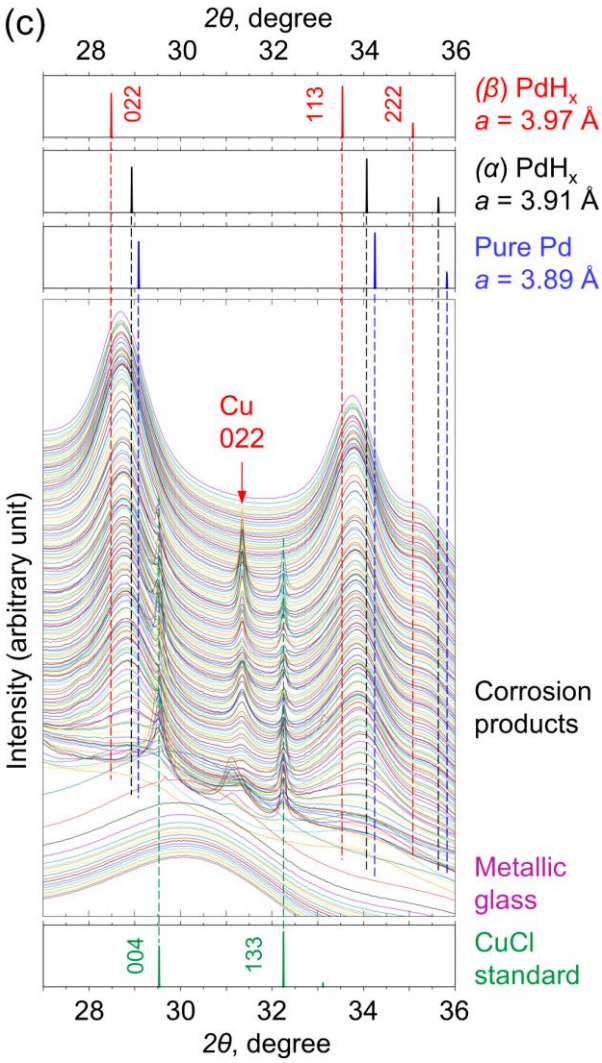

(see previous page for Figure 3 parts a and b)

Figure 3. Stacks of X-ray diffraction patterns collected at 3 μm spacing in an artificial pit on $Ti_{40}Zr_{10}Cu_{34}Pd_{14}Sn_2$ metallic glass in 0.9% NaCl: (a) at 0.5 V vs. Ag/AgCl at a distance of ~70 μm above the interface, (b) at 0 V vs. Ag/AgCl close to the interface, the *y* values are in reference to the *y* axis values in Figure 2d, and (c) at 0 V vs. Ag/AgCl from the metallic glass to a distance of ~420 μm from the interface. Also shown, for comparison: standard patterns for Pd, CuCl, Cu, $ZrOCl_2 \cdot 8H_2O$, Cu_2O, and two simulated patterns for Pd with larger lattice parameters (values in legend) to represent PdH_x. The pit depth is ≈1.8 mm. The pit was initially grown at 0.7 V.

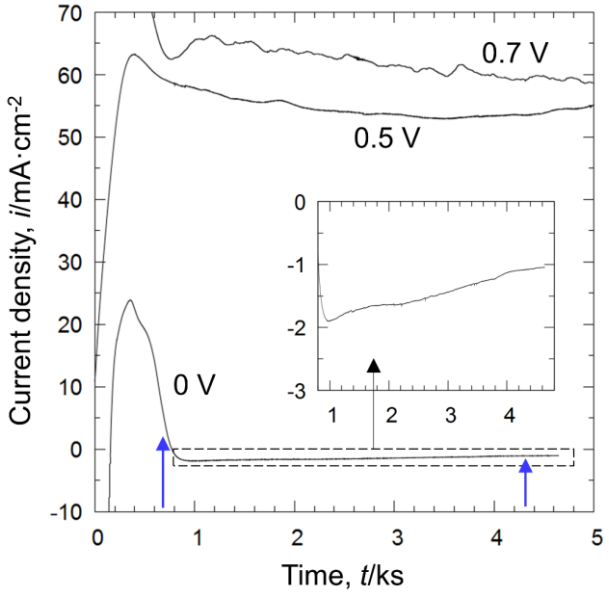

Figure 4. Current density-time evolution at applied constant potentials 0.7, 0.5 and 0 V for the artificial pit shown in Figure 2 ($Ti_{40}Zr_{10}Cu_{34}Pd_{14}Sn_2$ metallic glass foil in 0.9% NaCl). The two blue arrows pointing at the 0 V curve indicate the beginning and the end of the XRD scan shown in Figure 2d and 3c.

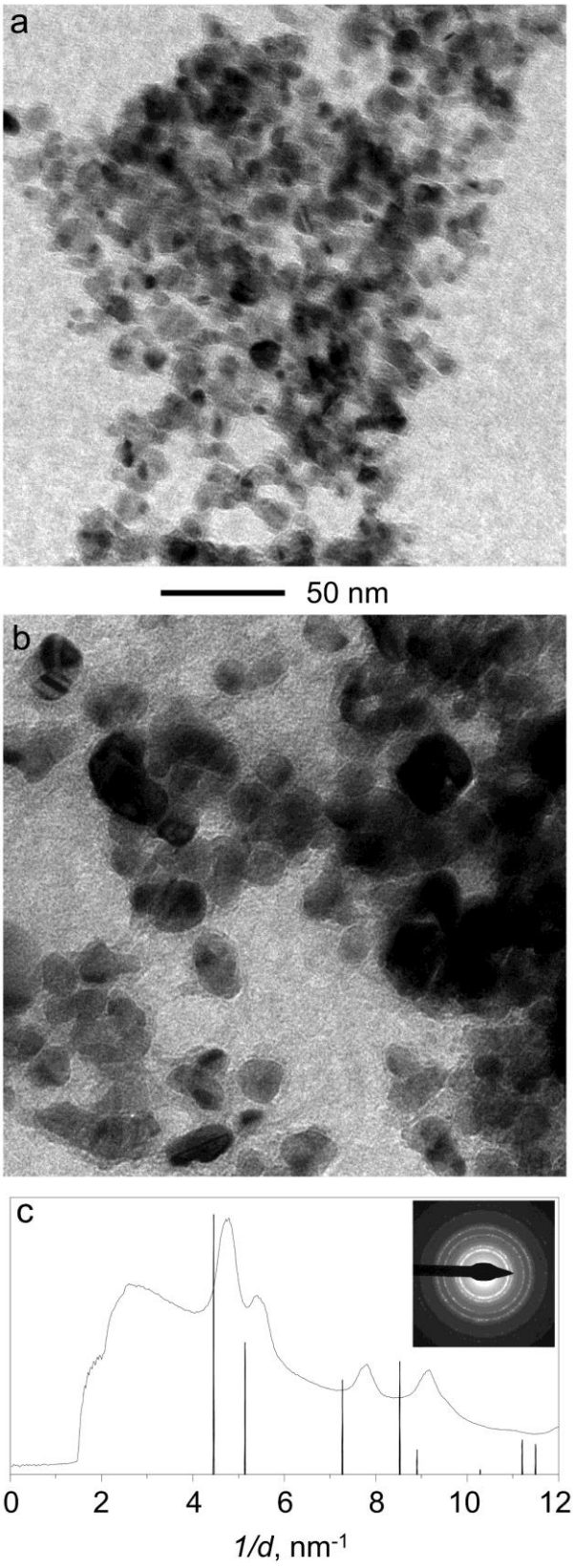

Figure 5. Bright field TEM images of corrosion products generated inside artificial pits on $Ti_{40}Zr_{10}Cu_{34}Pd_{14}Sn_2$ metallic glass ribbons in 0.9% NaCl at (a) 1.3 V for 4 h to a depth of ~1 mm, and (b) at 0.7 V for 4.3 h to a depth of ~1.2 mm (c) Diffraction pattern determined by azimuthal integration of the 2D electron diffraction pattern shown in the inset (0.7 V). Vertical lines represent Bragg reflections of standard Pd (a = 3.89 Å).

Table 1. Crystalline phases detected by in situ synchrotron X-ray diffraction inside artificial pits on $Ti_{40}Zr_{10}Cu_{34}Pd_{14}Sn_2$ metallic glass ribbons in given conditions. The pit at 0.5 and 0 V vs. Ag/AgCl was initially grown at 0.7 V.

Electrolyte	Applied potential [V vs. Ag/AgCl]	Pd	$PdCl_2$	CuCl	Cu	Others
PS[a)]		yes	yes	yes	-	'X1', 'X2', 'X3', 'X4'[d)]
PS + A[b)]	1.3	yes	yes	yes	-	'X1', 'X2', 'X3', 'X4'
PS + P[c)]		yes	yes	yes	-	'X1', 'X2', 'X3', 'X4'
PS + A + P		yes	yes	yes	-	'X1', 'X2', 'X3', 'X4'
PS	0.7	yes	-	yes	-	'X3', 'X4'
PS	0.5	yes	-	yes	yes	$ZrOCl_2 \cdot 8H_2O$, 'X4'
PS	0	yes	-	yes	yes	Cu_2O, PdH_x (?), 'X5', 'X6'

[a)]PS: NaCl (0.9%); [b)]A: albumin (4%); [c)]P: H_2O_2 (0.1%); [d)] 'X1', 'X2', 'X3' and 'X4' are unknown crystalline phases.

Table 2. Lattice parameter and crystallite size of Pd particles generated inside artificial pits on $Ti_{40}Zr_{10}Cu_{34}Pd_{14}Sn_2$ metallic glass ribbons. The pit at 0.5 and 0 V vs. Ag/AgCl was initially grown at 0.7 V. Lattice parameter and crystallite size determined from the 113 reflection. Lattice parameter of standard Pd taken from Inorganic Crystal Structure Database (ICSD), reference number 648675. The maximum and minimum lattice parameters of α- and β-PdH_x ($a(\alpha_{max})$ and $a(\beta_{max})$) nanoparticles (3 nm), respectively, from Ingham et al.[28]

Electrolyte/ Phase	Applied potential [V vs. Ag/AgCl]	Lattice parameter [Å]	Crystallite size [nm]	n[d)]
PS[a)]		3.891(5)	6.8 ± 0.9	82
PS + A[b)]	1.3	3.887(3)	6.9 ± 0.5	43
PS + P[c)]		3.890(4)	5.0 ± 0.6	63
PS + A + P		3.892(3)	6 ± 1	21
PS	0.7	3.887(5)	3.4 ± 0.4	70
PS	0.5	3.897(3)	2.9 ± 0.1	101
PS (interface)	0	3.908(5)	2.4 ± 0.1	5
PS (0.21 mm above interface)	0	3.932(1)	3.43 ± 0.02	5
PS (0.42 mm above interface)	0	3.9417(3)	3.76 ± 0.01	5
Standard pure Pd		3.89		
α-PdH_x ($a(\alpha_{max})$)		3.91	3	
β-PdH_x ($a(\beta_{min})$)		3.97	3	

[a)]PS: NaCl (0.9%); [b)]A: albumin (4%); [c)]P: H_2O_2 (0.1%); [d)] n: the number of individual measurements.

Table 3. Concentration values of chemical elements identified in the corrosion products generated inside artificial pits on $Ti_{40}Zr_{10}Cu_{34}Pd_{14}Sn_2$ metallic glass ribbon in 0.9% NaCl grown at 1.3 and 0.7 V for 4 h to a depth of ~1 mm and for 4.3 h to a depth of ~1.2 mm respectively. These were measured by EDX analysis on ten different particles.

Applied potential [V vs. Ag/AgCl]		Ti	Zr	Cu [at. %]	Pd	Sn
1.3	Mean	5±3	5±3	3±3	85±6	2±1
0.7	Mean	5±2	5±1	9±2	80±5	1±2

Recently developed biocompatible Ti-based bulk metallic glasses with high mechanical strength are promising candidates for use in small implants. Here, corrosion products generated in artificial pits on a promising Ti-based bulk metallic glass are investigated in situ with synchrotron X-ray diffraction. Results indicate that this metallic glass may release palladium or palladium hydride nanoparticles in service-relevant conditions with possible significant consequences on biocompatibility.

Metallic biomaterials

P. F. Gostin*, O. Addison, A. Morrell, Y. Zhang, A. Cook, A. Liens, M. Stoica, K. Ignatyev, S. R. Street, J. Wu, Y. L. Chen, and A. J. Davenport*

Palladium Nanoparticles Generated by Corrosion of a Ti-Based Bulk Metallic Glass for Implant Applications

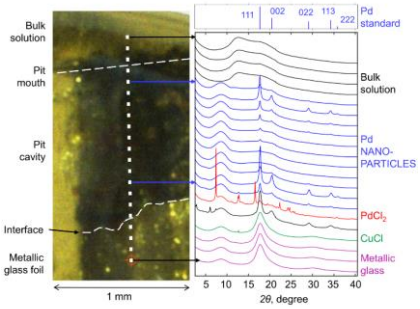

Supporting Information

Palladium Nanoparticles Generated by Corrosion of a Ti-Based Bulk Metallic Glass for Implant Applications

Petre Flaviu Gostin, Owen Addison, Alexander Morrell, Yue Zhang, Angus Cook, Alethea Liens, Mihai Stoica, Konstantin Ignatyev, Steven Richard Street, Jing Wu, Yu-Lung Chiu, and Alison J. Davenport**

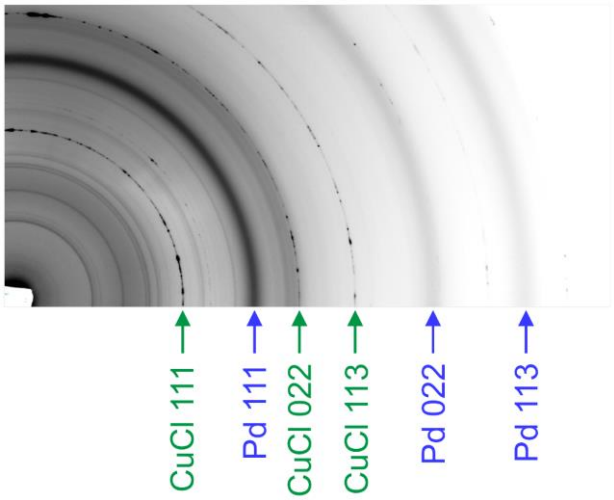

Figure S1. Raw two-dimensional diffraction pattern of corrosion products in an artificial pit on $Ti_{40}Zr_{10}Cu_{34}Pd_{14}Sn_2$ metallic glass in 0.9% NaCl at 1.3 V vs. Ag/AgCl. This pattern corresponds to pattern number 72 in Figure 1c, i.e. within a few tens of micrometres from the dissolving interface.

Additional information on unknown phases 'X1'-'X4'

In section 2.1.1, the presence of four different unknown phases 'X1' to 'X4' at 1.3 V in 0.9% NaCl was inferred from diffraction patterns because all the peaks attributed to each individual phase appear to increase and decrease together. This is illustrated in Figure S2 below. Figure S2(a) shows points 52-82 from the data set shown in Figure 1(c) in the main text showing the region close to the dissolving interface. It can be seen that peaks attributed to 'X1' and 'X2' are found at different locations from peaks attributed to 'X3' and 'X4'. The main 'X1' peak at 6.04° and the main 'X3' peak at 5.98° cannot be separated. However, the other 'X1' peak at 12.07° and 'X3' peaks, e.g. 8.28°, are clearly distinct and spatially separated. Figure S2(b) zooms in on the region where the main 'X1' and 'X2' peaks are located. It can be seen that the height of the main 'X1' peak at 6.04° is maximum at point 56 and decreasing with increasing point number. However, the height of the 'X2' peaks increases with point number from point 55 to 67.
Figure S2(c) shows a raw two-dimensional diffraction pattern corresponding to point 56. It can be seen that the main diffraction ring of 'X1' at 6.04° is uniform, while the main diffraction ring of 'X2' at 2.84° is less uniform suggesting these rings originate from two distinct phases. Figure S2(d) zooms in on the region where the main 'X3' and 'X4' peaks are located. The height of the 'X3' and 'X4' peaks is relatively small and these appear to increase and decrease together suggesting that 'X3' and 'X4' are one and the same phase. However, close inspection of Figure S2(d) reveals that red marked 'X3' peaks increase and decrease together reaching maximum height at point 72, while the green marked 'X4' peaks appear to increase and decrease together reaching a maximum at point 74. Further, it is noted that the 'X4' peaks appear to increase and decrease in a similar fashion to the CuCl peaks, which also reach maximum height at point 74.
Figure S3a shows a stack of diffraction patterns at 0 V close to the interface. As mentioned in the main text, most of the peaks have been attributed to Pd, CuCl, Cu_2O and Cu. Several minor peaks, indicated by small inclined arrows on patterns number 10 and 19, are attributed to two unknown phases 'X5' and 'X6'. It can be seen that all the peaks attributed to each individual phase appear to increase and decrease together. 'X5' has the highest peaks in pattern 10. 'X6' has the highest peaks in patterns 16 to 20. Figure S3b shows a raw two dimensional patterns corresponding to pattern 16 in Figure S3a. 'X6' and Cu_2O exhibit continuous and uniform diffraction rings suggesting randomly oriented crystallites. 'X5' exhibits less visible rings. It is not clear whether these too are continuous. In contrast, CuCl exhibits discontinuous and spotty rings indicating anisotropy.
As mentioned in Table 1 (in the main text), the unknown phases 'X1' to 'X4' appear to also be present at 1.3 V in 0.9% NaCl when albumin and/or H_2O_2 is added. Furthermore, 'X3' and 'X4' appear to be present at 0.7 V, while 'X4' is also seen at 0.5 V. 'X5' and 'X6' are present at 0 V. Representative diffraction patterns for each unknown phase are shown in Figure S4. Figure S4 also shows the standard diffraction patterns for several phases which can be expected considering the alloy composition: $ZrOCl_2 \cdot 6H_2O$ (ICDD, reference number 00-047-0815), TiO_2 anatase (ICSD, 202242), TiO_2 rutile (ICSD 202240), $CuCl_2$ (ICSD 26667), $CuCl_2 \cdot 2H_2O$ (ICSD 40290), $SnCl_2$ (ICSD 15452). It can be seen that none of the mentioned phases satisfactorily match the peaks attributed to 'X1'-'X6'.

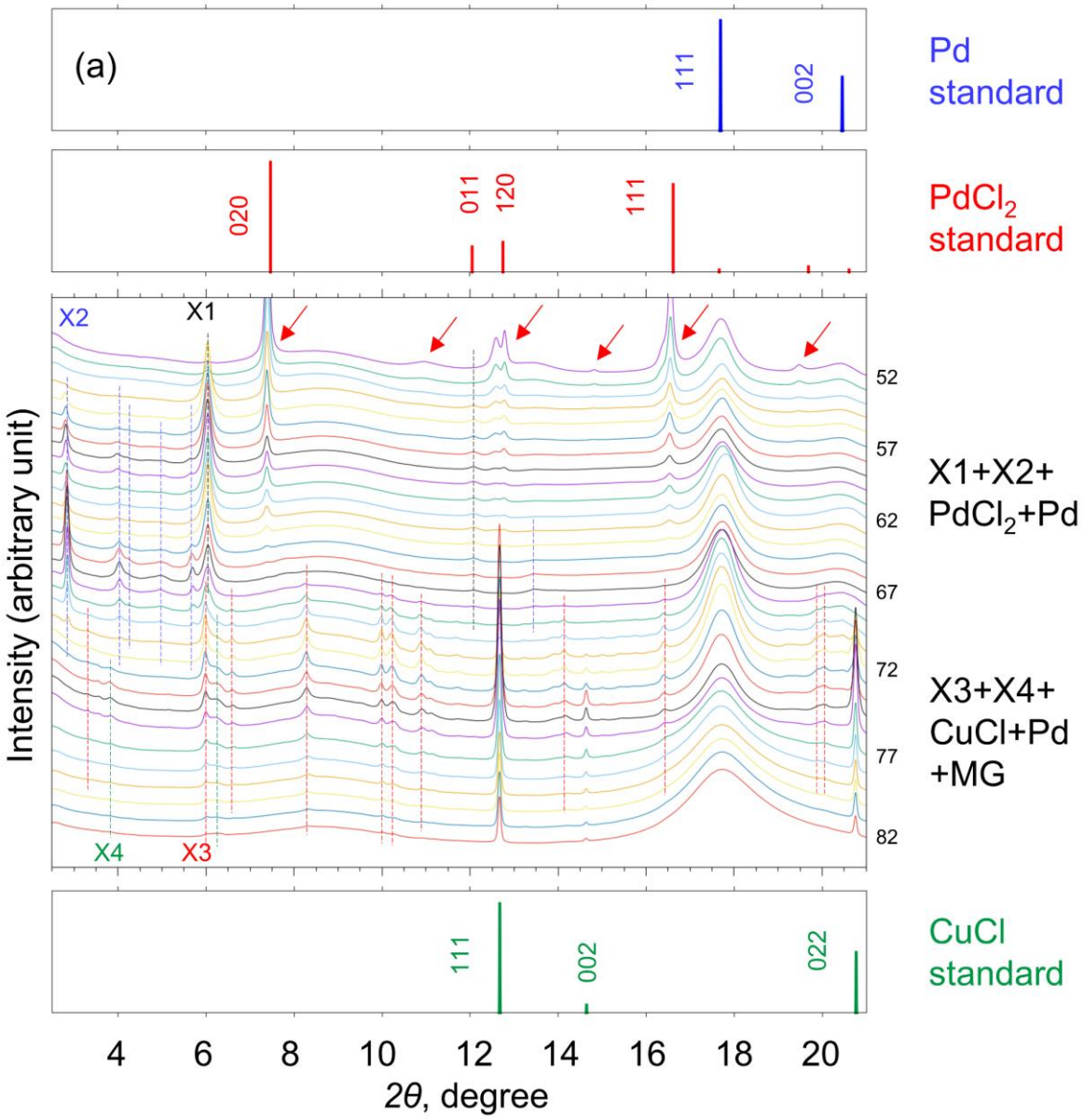

Figure S2. XRD patterns of corrosion products inside an artificial pit cavity on $Ti_{40}Zr_{10}Cu_{34}Pd_{14}Sn_2$ metallic glass in 0.9% NaCl at 1.3 V. Patterns were collected at 5 µm spacing. (a) Same as Figure 1c (in the main text) zoomed in on points 52 to 82, (b) same as subfigure 'a' zoomed in on points 52 to 72, (c) raw two-dimensional pattern corresponding to point 56 in previous subfigures, (d) same as subfigure 'a' zoomed in on points 67-82. Inclined red arrows indicate peaks attributed to $PdCl_2$. Vertical broken lines indicate the position of peaks attributed to unknown phases 'X1' (black), 'X2' (blue), 'X3' (red) and 'X4' (green).

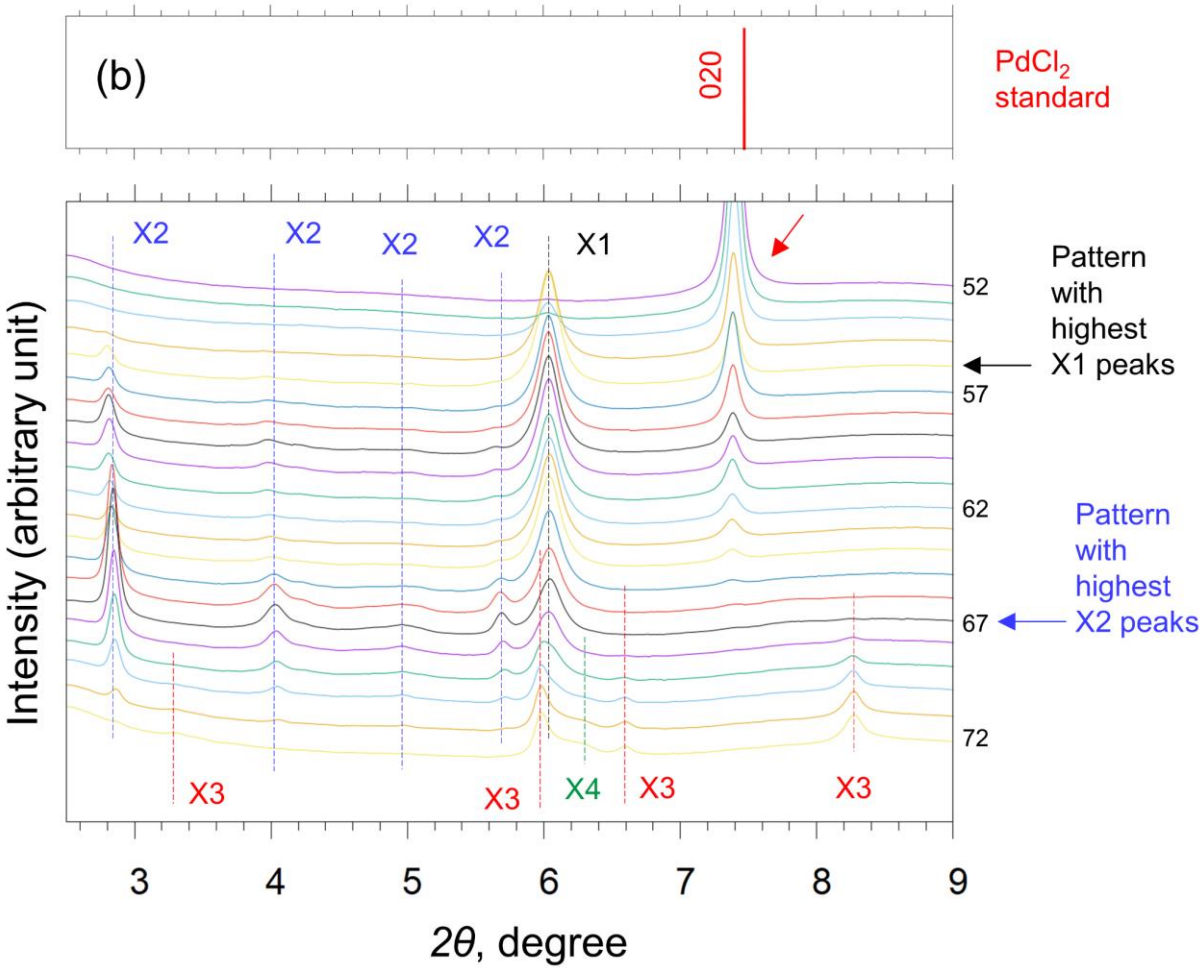

Figure S2. XRD patterns of corrosion products inside an artificial pit cavity on $Ti_{40}Zr_{10}Cu_{34}Pd_{14}Sn_2$ metallic glass in 0.9% NaCl at 1.3 V. Patterns were collected at 5 µm spacing. (a) Same as Figure 1c (in the main text) zoomed in on points 52 to 82, (b) same as subfigure 'a' zoomed in on points 52 to 72, (c) raw two-dimensional pattern corresponding to point 56 in previous subfigures, (d) same as subfigure 'a' zoomed in on points 67-82. Inclined red arrows indicate peaks attributed to $PdCl_2$. Vertical broken lines indicate the position of peaks attributed to unknown phases 'X1' (black), 'X2' (blue), 'X3' (red) and 'X4' (green).

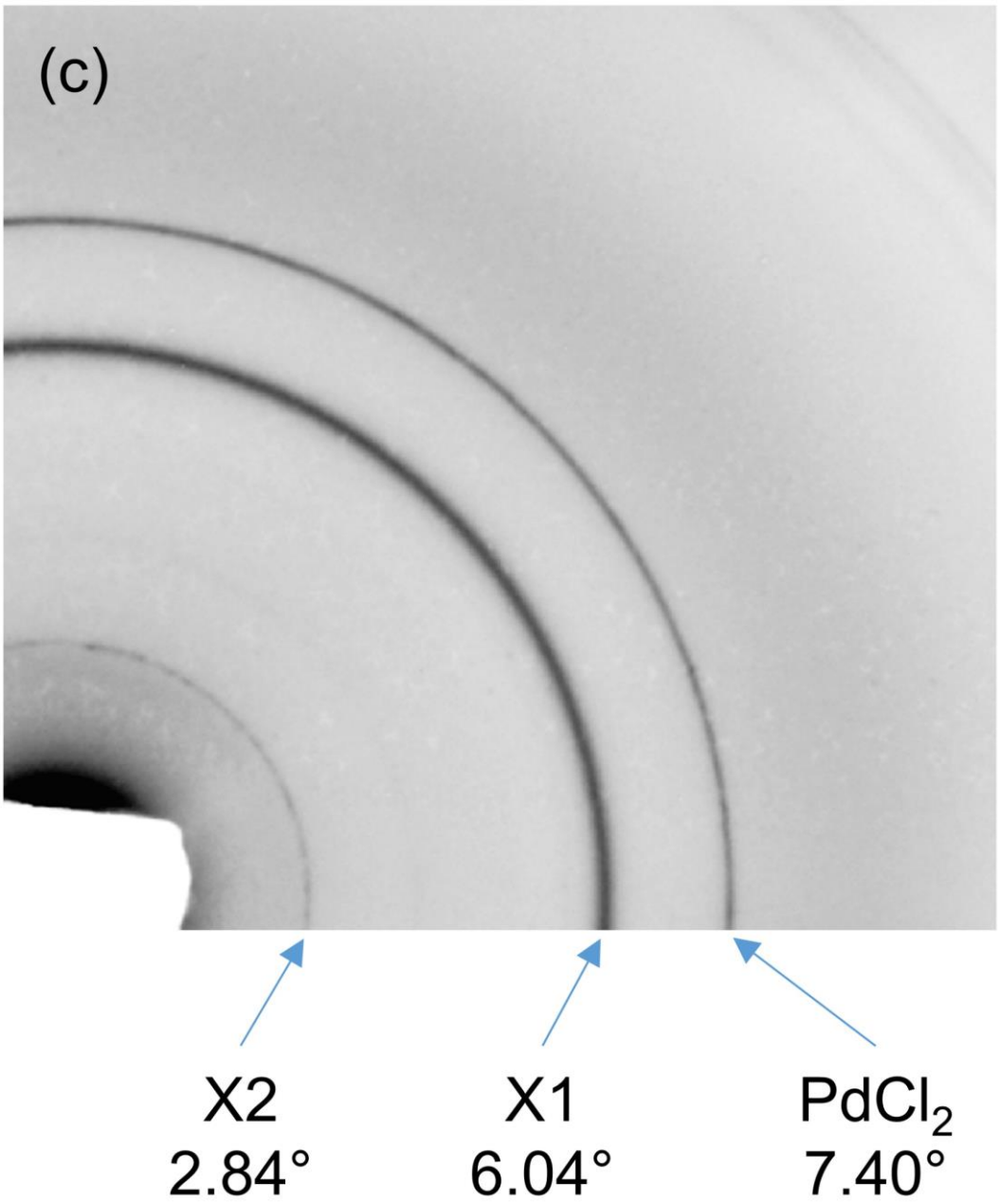

Figure S2. XRD patterns of corrosion products inside an artificial pit cavity on $Ti_{40}Zr_{10}Cu_{34}Pd_{14}Sn_2$ metallic glass in 0.9% NaCl at 1.3 V. Patterns were collected at 5 µm spacing. (a) Same as Figure 1c (in the main text) zoomed in on points 52 to 82, (b) same as subfigure 'a' zoomed in on points 52 to 72, (c) raw two-dimensional pattern corresponding to point 56 in previous subfigures, (d) same as subfigure 'a' zoomed in on points 67-82. Inclined red arrows indicate peaks attributed to $PdCl_2$. Vertical broken lines indicate the position of peaks attributed to unknown phases 'X1' (black), 'X2' (blue), 'X3' (red) and 'X4' (green).

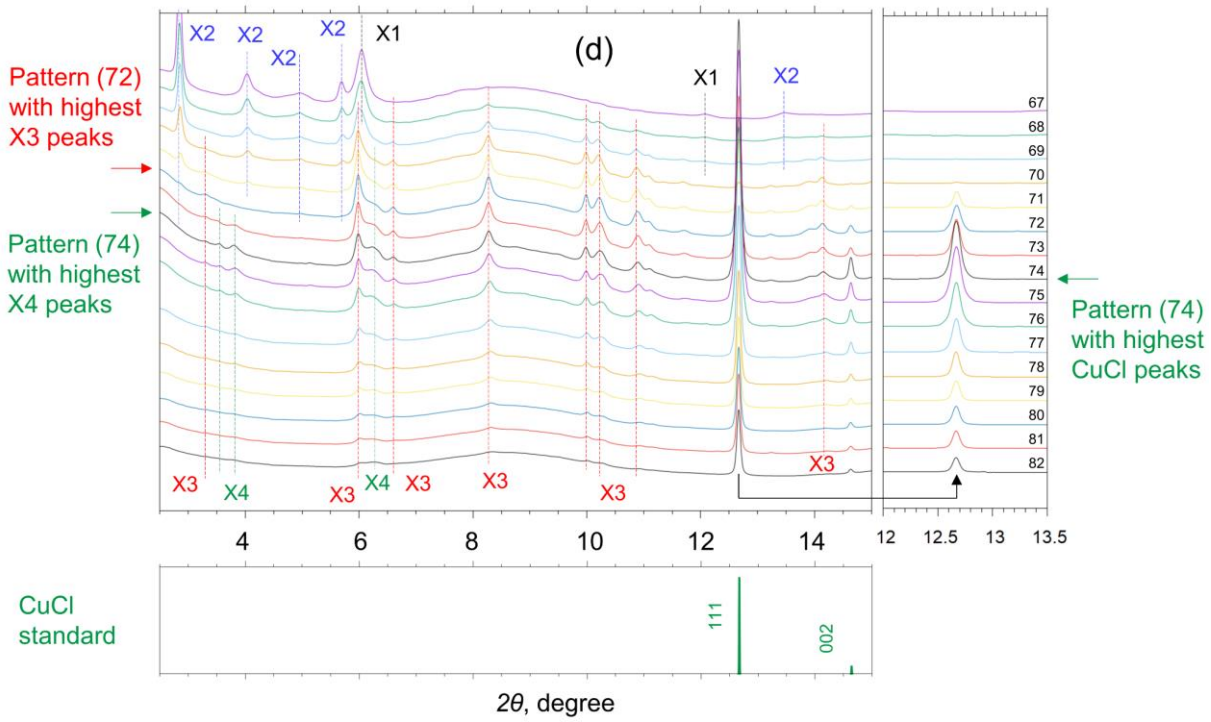

Figure S2. XRD patterns of corrosion products inside an artificial pit cavity on $Ti_{40}Zr_{10}Cu_{34}Pd_{14}Sn_2$ metallic glass in 0.9% NaCl at 1.3 V. Patterns were collected at 5 µm spacing. (a) Same as Figure 1c (in the main text) zoomed in on points 52 to 82, (b) same as subfigure 'a' zoomed in on points 52 to 72, (c) raw two-dimensional pattern corresponding to point 56 in previous subfigures, (d) same as subfigure 'a' zoomed in on points 67-82. Inclined red arrows indicate peaks attributed to $PdCl_2$. Vertical broken lines indicate the position of peaks attributed to unknown phases 'X1' (black), 'X2' (blue), 'X3' (red) and 'X4' (green).

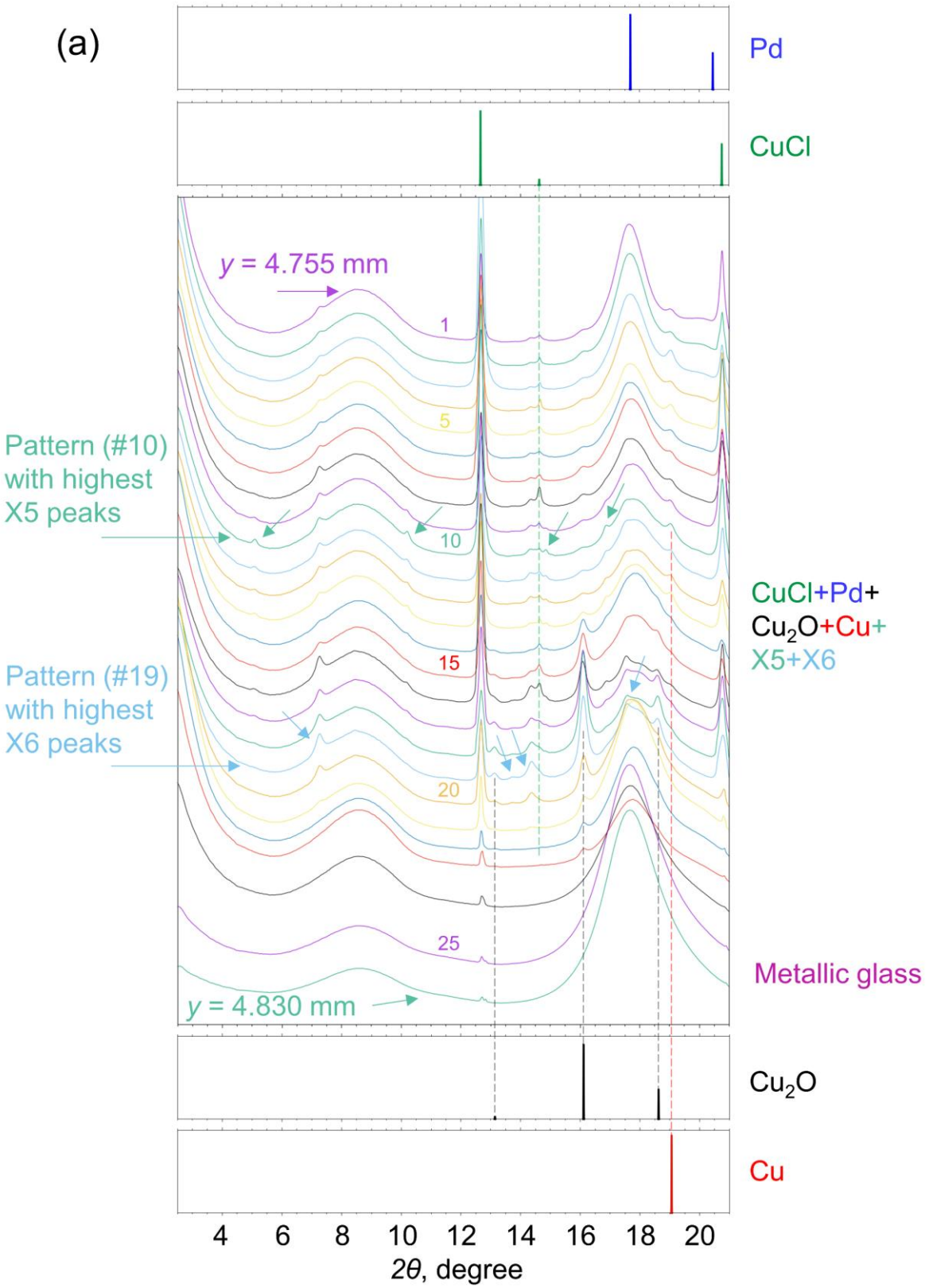

Figure S3. (a) Stack of diffraction patterns of corrosion products inside an artificial pit cavity on $Ti_{40}Zr_{10}Cu_{34}Pd_{14}Sn_2$ metallic glass in 0.9% NaCl at 0 V compared with standard patterns for Pd, CuCl, Cu_2O and Cu. These are the same patterns shown in Figure 3b. The *y* values are in reference to the *y* axis values in Figure 2d. Patterns were collected at 3 µm spacing. The arrows on patterns number 10 and 19 indicate peaks attributed to unknown phases 'X5' and 'X6', respectively; (b) raw two-dimensional pattern corresponding to pattern number 16 in subfigure (a).

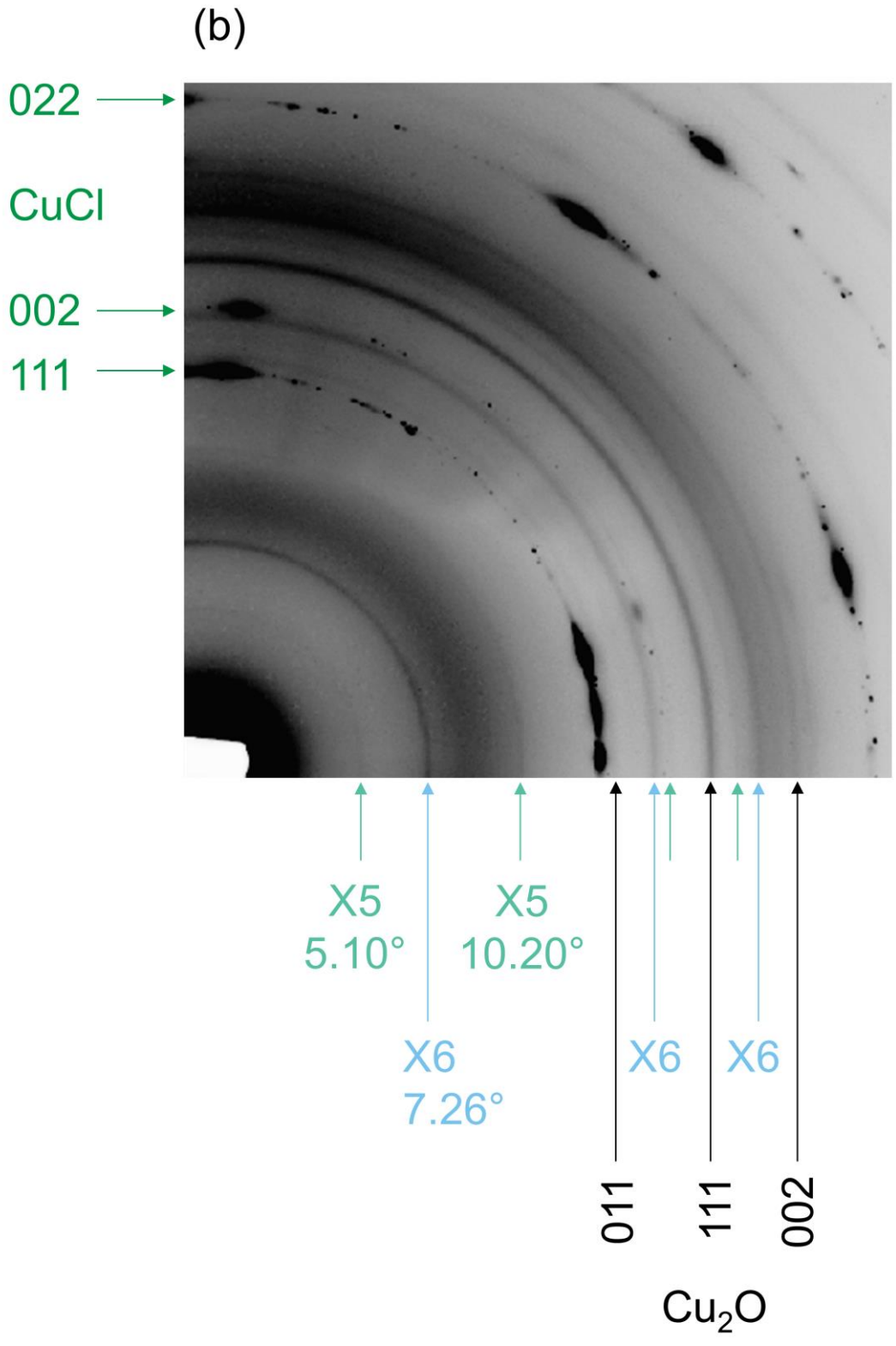

Figure S3. (a) Stack of diffraction patterns of corrosion products inside an artificial pit cavity on $Ti_{40}Zr_{10}Cu_{34}Pd_{14}Sn_2$ metallic glass in 0.9% NaCl at 0 V compared with standard patterns for Pd, CuCl, Cu_2O and Cu. These are the same patterns shown in Figure 3b. The *y* values are in reference to the *y* axis values in Figure 2d. Patterns were collected at 3 µm spacing. The arrows on patterns number 10 and 19 indicate peaks attributed to unknown phases 'X5' and 'X6', respectively; (b) raw two-dimensional pattern corresponding to pattern number 16 in subfigure (a).

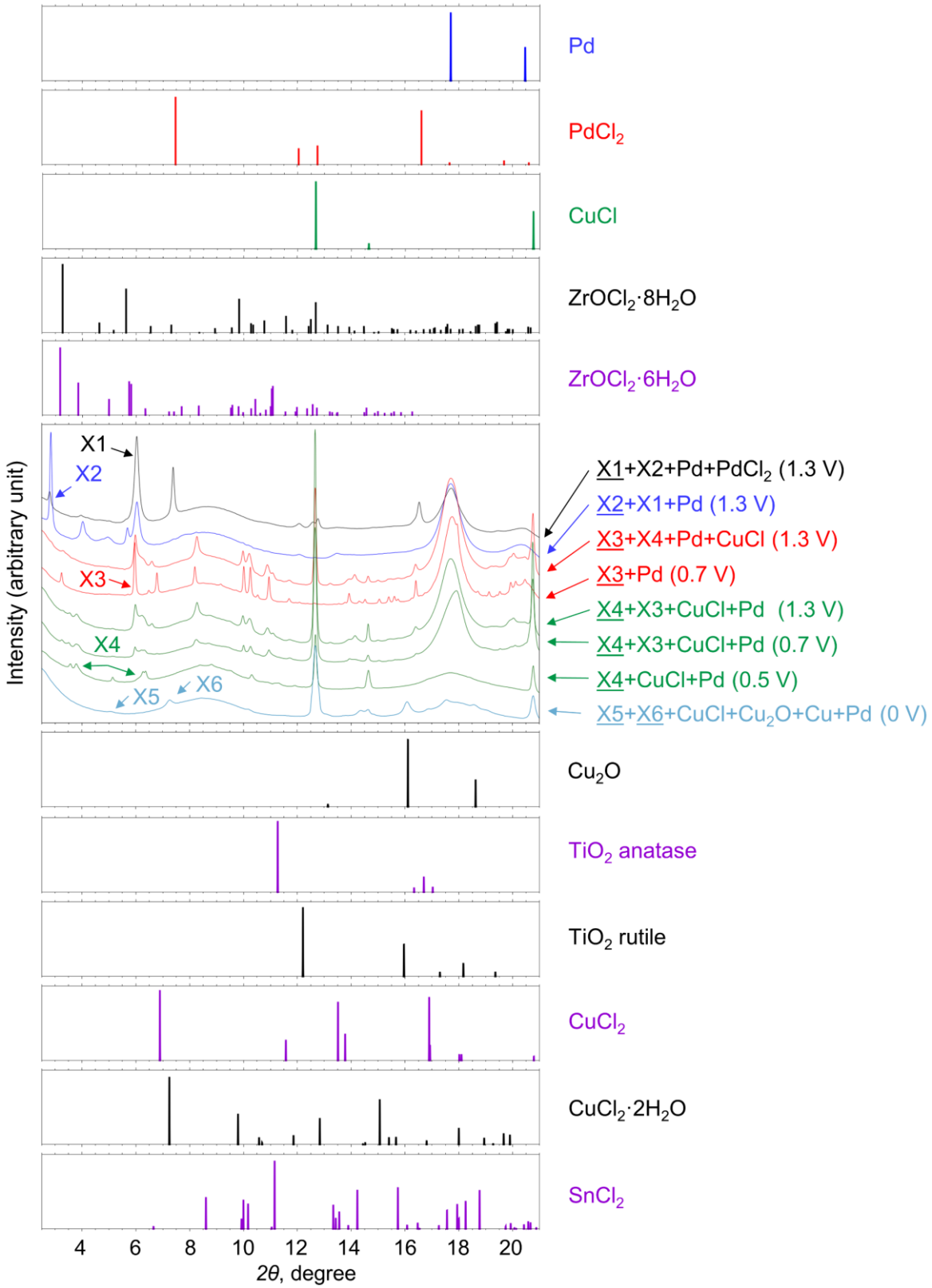

Figure S4. Selected individual XRD patterns of corrosion products inside artificial pit cavities on $Ti_{40}Zr_{10}Cu_{34}Pd_{14}Sn_2$ metallic glass in 0.9% NaCl (+4% albumin, +0.1% H_2O_2) at 1.3, 0.7 0.5 and 0 V. The selected patterns have the highest peaks of each of the unknown phases 'X1' to 'X6' (underlined in legend).The main peaks of each of the unknown phases are indicated. Also shown: standard patterns of Pd, $PdCl_2$, CuCl, $ZrOCl_2·8H_2O$, $ZrOCl_2·6H_2O$, Cu_2O, TiO_2 anatase, TiO_2 rutile, $CuCl_2$, $CuCl_2·2H_2O$ and $SnCl_2$.

Polarisation behaviour of artificial pits and visual appearance of corrosion products

Pits were initially grown at potentials of 0.7 V or higher. Pits could not be initiated reliably at lower potentials. After the pits reached a depth of several hundred micrometres, cyclic polarisation curves and concurrent time lapses were recorded. Figure S5 shows a typical current - potential curve and selected images of an artificial pit in 0.9% NaCl grown initially at 0.7 V to a depth of approximately 0.4 mm. During the growth period at 0.7 V, a thick black layer of corrosion products is formed (see Figure S5, images 'A'). As the pit grows in depth, the black layer moves down with the receding electrode surface. It is formed of fine particles which tend to aggregate, but it is not very compact as occasional bubbles formed underneath can escape relatively easily. It may be seen in Figure S5 (images 'A') that a lighter substance forms within the black layer close to the dissolving interface.
Current-potential curves show relatively poor repeatability with significant current noise as seen in Figure S5. There is considerably less noise for ribbons embedded in thick epoxy resin (not shown here), suggesting that the noise for ribbons embedded in thin Araldite epoxy (required for synchrotron experiments) is attributed to corrosion products causing local wedging of the Araldite epoxy exposing fresh metal surface. As the potential is swept down from 0.7 V (point 'A'), the current first decreases to a minimum at 0.5-0.6 V (point 'B') and then increases to a maximum at 0.2-0.3 V (point 'C'). It then decreases down to a negligible current value at 0 V in a more or less linear fashion consistent with growth under ohmic control. Below 0.03 V (point 'D') the interface appears to stop advancing indicating a significant decrease of the dissolution rate, probably due to repassivation, which is consistent with the low measured current in that potential region. Upon sweeping up the potential, the current maintains low values until reactivation of the pit takes place and the current suddenly increases at 0.3 V (point 'E') and then more gradually up to 0.6 V (point 'F'). At 0.4 V, the light layer starts to thin down from its top side and disappears completely at 0.8 V (compare images 'D' and 'F'). Meanwhile, the interface appears to start advancing visibly again when the potential reaches a value of 0.6 V, corresponding to the abrupt and massive increase in current at point 'F'. Between 0.7 and 1.3 V, the interface has a bright appearance. Figure S5 (image 'G') shows an image at 0.9 V, at which the interface displays maximum brightness (point 'G'). From 1.6 V up to 1.8 V (upper scan limit) and down to 1.3 V, considerable gas evolution takes place. The gas evolution leads to fragmentation of the corrosion products and much of those are being pushed out of the pit cavity into the bulk electrolyte (see Figure S5, image 'H'). During the time gas evolution takes place, the interface does not advance significantly. Going further, below 1.3 V, visible dissolution occurs again and the process is repeated in subsequent cycles.

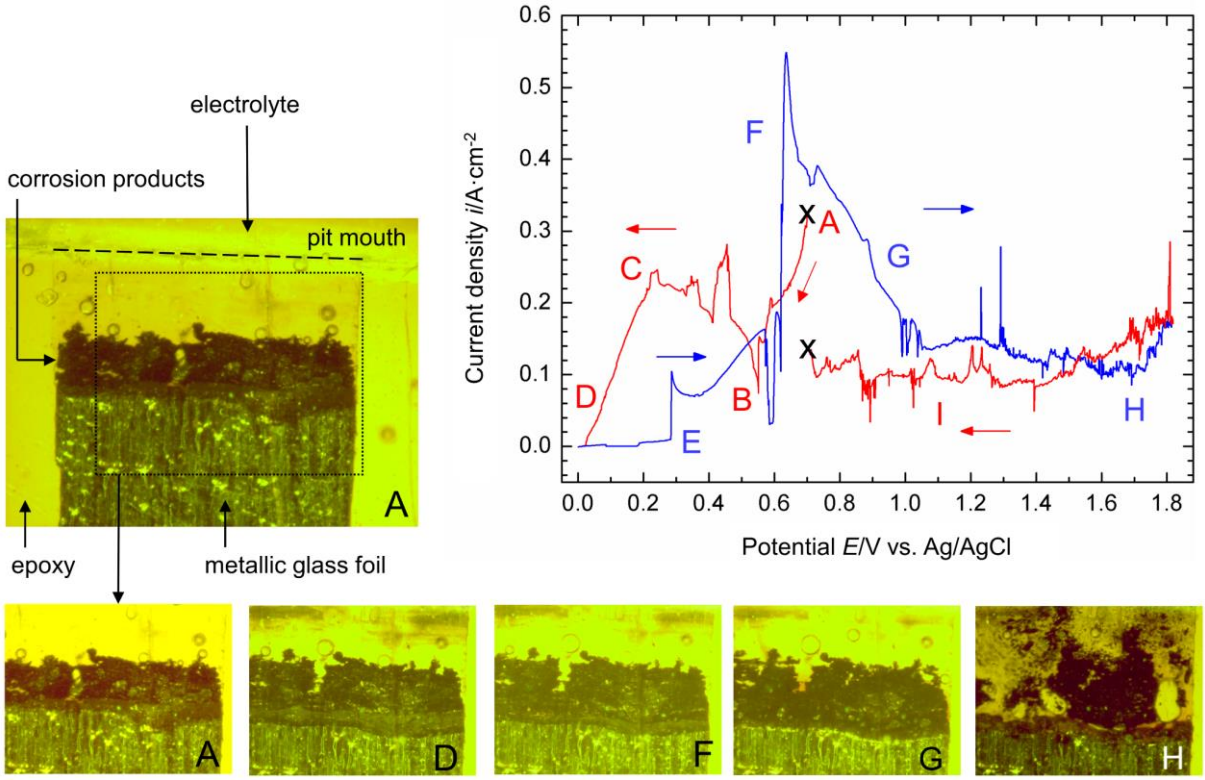

Figure S5. Cyclic polarisation curve for an artificial pit on $Ti_{40}Zr_{10}Cu_{34}Pd_{14}Sn_2$ metallic glass in 0.9% NaCl. The pit was initially grown at constant potential 0.7 V for ≈40 min (depth ≈0.4 mm). Also shown, optical microscope images of the artificial pit at points indicated on the polarisation curve.